Anita Weidinger, BSc

Reverse annealing in the LHZ-model

Master's Thesis

to achieve the university degree of

Diplom-Ingenieurin

Master's degree programme: Technical Physics

submitted to

Graz University of Technology

Supervisor

Ao. Univ. Prof. Hans Gerd Evertz

Institute of Theoretical and Computational Physics
TU Graz

Co-Supervisor

Ass.-Prof. Dr. Wolfgang Lechner
Institute for Theoretical Physics, University of Innsbruck

Graz, May 2020

This document is set in Palatino, compiled with pdfLaTeX2e and `Biber`.

The LaTeX template from Karl Voit is based on KOMA script and can be found online: https://github.com/novoid/LaTeX-KOMA-template

Affidavit

I declare that I have authored this thesis independently, that I have not used other than the declared sources/resources, and that I have explicitly indicated all material which has been quoted either literally or by content from the sources used. The text document uploaded to TUGRAZonline is identical to the present master's thesis.

Date	Signature

Acknowledgements

I want to especially thank my supervisor in Innsbruck, Wolfgang Lechner, for this great opportunity and his continuous support throughout the thesis. I also want to thank my supervisor in Graz, Hans G. Evertz, for useful discussions and advice.
Furthermore, great thanks go to Andreas Hartmann, who helped me at different stages of my project, especially the analytical part. I also appreciated the discussions with Martin Lanthaler and want to thank the whole 'Quantum Optimization' group for the good work environment.
Also, I want to thank Roeland for everything, especially his (almost) never-ending patience.
Last but not least, I want to thank my parents for their great support even if they don't know what I am doing.

Abstract

With quantum annealing it is possible to solve optimization problems. Current research is focused on improving the originally proposed method. One modification is reverse annealing. In this thesis we will implement reverse annealing in the LHZ-model. The LHZ-model is a quantum annealing architecture that implements all-to-all connectivity as local fields. The classical starting state is chosen to be the ground state of the local field term of the LHZ-Hamiltonian. With an analytically derived expression for the magnetization we can show that reverse annealing can avoid/weaken the effect of a first-order phase transition. Numerical work shows that a new problem arises with close energy gaps due to the chosen initial Hamiltonian. With a rescaling of the coefficients of the initial Hamiltonian, reverse annealing can outperform conventional quantum annealing. Furthermore, we can show that the constraint term of the LHZ-model has a significant influence on the annealing performance. With a quadratic drive of the constraint Hamiltonian the energy gap occurs later than with the linear drive. A quadratic drive also increases the size of the gap. In addition to the ground state fidelity, we also use the energy variance as a measure of the performance of the annealing runs.

Kurzfassung

Mit ‚Quantum Annealing' ist es möglich Optimierungsprobleme zu lösen. Die Methode befindet sich weiter in Entwicklung. Eine mögliche Modifikation ist ‚Reverse Annealing'. In dieser Arbeit wird diese Methode im sogenannten LHZ-Modell implementiert. Im LHZ-Modell entsprechen die Wechselwirkungen, die im Ising Modell auftreten, lokalen Feldern. In der Arbeit wird zuerst analytisch eine Gleichung für die Magnetisierung hergeleitet, die beweist, dass ‚Reverse Annealing' einen Phasenübergang erster Ordnung schwächen oder umgehen kann. Nimmt man den Grundzustand des lokalen Termes des LHZ-Hamiltonians als Startzustand, so bekommt man in den Simulationen dichte Eigenenergien am Anfang der Annealingprozedur, die die Performance deutlich verringern. Um das zu umgehen, wird der Koeffizient des lokalen Terms modifiziert. Dadurch kann ‚Reverse Annealing' ‚Quantum Annealing' an Performance übertreffen. Des Weiteren wird gezeigt, dass der ‚Constraint' Term des LHZ-Hamiltonians einen starken Einfluss auf das Ergebnis hat. Startet man den Term langsamer, so kann man ‚Reverse Annealing' weiter verbessern. Das liegt daran, dass durch das langsame Starten des ‚Constraint' Terms die minimale Energielücke zwischen Grundzustand und erstem angeregten Zustand später auftritt und sich auch vergrößert. Als Maß für die Performance verwenden wir die ‚Fidelity'. Am Ende analysieren wir die Ergebnisse auch mit der Varianz der Energie.

Contents

1 Introduction

The aim of quantum annealing is to solve classical combinatorial optimization problems via quantum fluctuations [1, 2]. These kind of problems appear in a large area of fields like computer science [3, 4], quantum chemistry [5], finance [6], machine learning [7, 8] and protein folding [9, 10]. To solve those problems one needs to find the minimum of a cost function, but very often they have a lot of local minima, which makes them hard to solve for classical algorithms. Quantum annealers are quantum devices designed to solve this challenging task.[2, 11]. The description of how quantum annealers work can be found in section 2.3.
A lot of research has been done in this field nevertheless, there are still big challenges that need to be overcome to gain a definite quantum speedup. [12–17]. A major problem, the minimal energy gap, can be found in more detail in section 2.3.2.
Different modifications of quantum annealing (QA) have been proposed to improve the performance of the original method, one of them is reverse annealing (RA) [18, 19]. RA is explained in section 2.3.3.
Not just the method, also the architecture of a quantum computer is open to innovations. While in common models, like the spin-glass model, difficulties like the all-to-all connectivity arise, another model, the LHZ-model, has been developed to avoid this problem. Further information about this can be found in section 2.4.
This thesis aims to implement RA on the LHZ-model and compare the performance to the conventional QA method.
To avoid confusion we also want to mention that this thesis deals with 'adiabatic quantum computing', which is strictly based on adiabatic processes. 'Quantum annealing' also includes noisy environments (e.g. from thermal sources) and diabatic transitions. The term 'quantum annealing' covers a broader field but, we will use this term in this thesis.
In the next section we want to introduce the chapters of this thesis.

1.1 Thesis outline

We will start with the theoretical background in chapter 2. The first section, section 2.2, provides basic knowledge of quantum mechanics and optimization problems. This is followed by an overview of quantum annealing, 2.3, with an explanation of the challenge of the minimal energy gap, 2.3.2, and a possible solution 'reverse annealing', 2.3.3. In the last section of this chapter, section 2.4, we introduce the LHZ-model, which helps to overcome other difficulties in quantum

annealing.
Chapter 3 is the analytical part of this thesis. There we can find the derivation of the free energy and magnetization of our system. The obtained equation is used later, in section 5.1, to gain useful information about the magnetization landscape.
The next chapter, 4, forms the foundation for the numerical part. Section 4.1 introduces the Hamiltonian for reverse annealing in the LHZ-model. It is followed by some information about the units, section 4.2. Finally, the whole set-up for the simulations is given in section 4.3. Here we give an overview of the several investigated cases.
Chapter 5 contains the outcome of analytical and the numerical investigations of reverse annealing in LHZ. Section 5.1 is based on the equation derived in chapter 3. We can see the magnetization landscape and when a jump in magnetization occurs. The next sections deal with the numerical results: the ground state fidelity, 5.2, the minimal energy gap, 5.3, and the variance of energy, 5.4. In the last chapter 6 we discuss the obtained results and give suggestions for future work.

2 Theoretical background

This chapter provides the theoretical background for this thesis. As reverse annealing aims to solve optimization problems we first want to give a brief overview of such problems. Then we summarize the most important parts of quantum mechanics before we give information about quantum annealing and its challenges. The LHZ-model is described in the last section.

2.1 Optimization problems

In optimization problems one seeks to find the best solution to a problem. Examples are timetables or transportation models where one needs to minimize shipping costs but also demands, capacities and supplies. Such problems are defined by N parameters. These N parameters can take different values. One set of parameters is called a configuration or state. To every configuration we can assign a *cost* via a *cost-function*. All configurations span up the configuration or state space. They also define the corresponding 'cost-landscape' of the optimization problem. An example is shown in figure 2.1. The configuration with the lowest costs is the solution to the problem.
There are classical algorithms that aim to solve such problems. They do well in smooth regions, like in the left of our landscape, figure 2.1. In rough regions, the right side, it can be problematic. This is the region where quantum tunneling is of advantage. This quantum phenomenon is described in the next section (2.2).

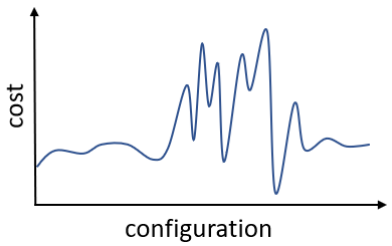

Figure 2.1: Example of a cost-function over different configurations.

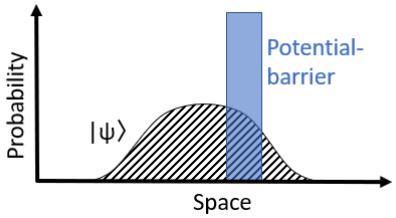

Figure 2.2: Example of a state $|\psi\rangle$ and a potential barrier.

2.2 Basic quantum mechanics

In quantum mechanics, states are described by a wave function $|\psi\rangle$ in Dirac notation. $|\psi\rangle$ is the 'ket' and $\langle\psi|$ is the 'bra' vector, which is the complex conjugate of the 'ket' vector.
Energies in a quantum mechanical system are quantized, which means that there are discrete energy levels, called **eigenenergies**. To every eigenenergy E_i corresponds a **eigenstate** $|\Phi_i\rangle$. The letter i labels the levels from 0 to the highest one. The ground state E_0 returns the lowest energy and higher energies are called excited states (E_1, E_2, E_3,...).
States can be expressed in a linear combination of the eigenstates like $|\psi\rangle = a\,|\Phi_0\rangle + b\,|\Phi_2\rangle + c\,|\Phi_3\rangle$. The state $|\psi\rangle$ is in **superposition** of the ground state and the second and third excited state as long as a, b and c are not 0. After a measurement the state $|\psi\rangle$ collapses into one of the 3 eigenstates, with respective probabilities $|a|^2$, $|b|^2$ and $|c|^2$.
As mentioned before a state $|\psi\rangle$ is described as a wave function. An example is shown in figure 2.2. Let $|\psi\rangle$ be the wavefunction of a photon. The photon has different probabilities of existence over the space. In the potential barrier, which we can relate to a thin peak in figure 2.1, the photon has 0 probability of existence. This also holds for classical particles. Nevertheless, it has a small probability to be on the other side of the barrier. This means that quantum particles can **tunnel** through the barrier, a classical algorithm would have to 'climb' the potential first. The tunneling rate is related to the thickness of the barrier. This is of major advantage in rough regions as seen in figure 2.1 [20].
An interesting article about a hybrid algorithm of a classical and quantum algorithm is [21], which uses reverse annealing (section 2.3.3) as a local search.

2.2.1 Fidelity

The fidelity gives information to which degree two states overlap with each other. A fidelity of 1 means that the two states are identical.
In this thesis we are dealing with a so-called 'evolving state' $|\psi\rangle$ and we are interested in the ground state $|\Phi_0\rangle$ of a system. The ground state fidelity gives a measure of how much $|\psi\rangle$ overlaps with $|\Phi_0\rangle$ and is defined in this thesis as follows:

$$F := |\langle \psi | \Phi_0 \rangle|^2 \tag{2.1}$$

We can also relate to other states, e.g. to the excited states ($|\Phi_1\rangle$, $|\Phi_2\rangle$, $|\Phi_2\rangle$,...) of the system.

2.3 Quantum annealing (QA)

QA exploits quantum mechanics (quantum tunneling) to achieve a speedup over classical algorithms. This means that the optimization problems need to get lifted into the quantum regime. This is done by encoding it in a Hamiltonian, not a cost function. A function with a lot of local minima is shown to translate to a spin glass Ising-Hamiltonian [22]. Some examples of how to map a problem onto such a model are shown in [23]. Now we can write down the Problem-Hamiltonian as

$$\hat{H}_P = -\sum_{i=1}^{N}\sum_{j<i} J_{ij}\hat{\sigma}_i^z\hat{\sigma}_j^z - \sum_{i=1}^{N} b_i\hat{\sigma}_i^z. \tag{2.2}$$

The optimization problem is encoded in the interactions J_{ij} and in the external field b_i. The z-Pauli matrix $\hat{\sigma}^z$ refers to the N qubits in the quantum annealer. [2] One important foundation of quantum annealing is the adiabatic theorem. It states that a system stays in its instantaneous eigenstate (e.g. ground state) if the system evolves slow enough [24, 25]. This leads to the idea to initialize a system in the ground state of an 'easy-to-prepare' Hamiltonian $\hat{H}_1$ and then change it slowly to the 'difficult' Problem-Hamiltonian $\hat{H}_p$ (Equation 2.2). The measurement of the qubits will provide the desired solution. This sweep is described by the Hamiltonian

$$\hat{H}(t) = (1 - s(t))\hat{V}_{TF} + s(t)\hat{H}_P \tag{2.3}$$

where $s(t)$ rises from 0 to 1 over time. It is common to use a transverse field $-\sum_{i=1}^{N}\hat{\sigma}_i^x$ with $\hat{\sigma}^x$ as the x-Pauli matrix for $\hat{V}_{TF}$ [11].
The starting state of the annealing procedure is the ground state of the transverse field $\hat{V}_{TF}$ which is a superposition of all possible states. Furthermore the transverse field regulates the fluctuations which allows the state to explore the configuration space via quantum tunneling. This means that the transverse field can be understood as the analogon to the temperature in the classical counterpart of QA: simulated annealing.

2.3.1 Adiabatic theorem

The adiabatic theorem was first stated by Born M. and Fock V. in 1928 in the 'Zeitschrift für Physik' and is, as mentioned in the previous chapter, one of the important theoretical foundations of quantum annealing [24, 25]. It states that preparing a state at time $t = 0$ in the ground state $|\Phi_0(0)\rangle$ of the Hamiltonian $\hat{H}(0)$ and then evolving it according to the Schrödinger equation $\hbar\frac{\mathrm{d}}{\mathrm{d}t}|\psi(t)\rangle = \hat{H}(t)|\psi(t)\rangle$ the actual state $|\psi(t)\rangle$ at time t will correspond to $|\Phi_0(t)\rangle$. This holds for the assumptions that $\hat{H}(t)$ changes 'gradually' and there are no level crossings. [24] The change in $\hat{H}(t)$ is slow enough if

$$\max_{0\leq t\leq\tau}\frac{\left|\langle\Phi_i(t)|\frac{\mathrm{d}\hat{H}(t)}{\mathrm{d}t}|\Phi_0(t)\rangle\right|}{\Delta E_{i,0}(t)^2}\ll 1\quad(i\geq 1) \tag{2.4}$$

is satisfied. $\Delta E_{i,0}$ is the energy gap between the ground and the i-th excited state. One can rewrite this equation 2.4 in terms of $s(t) = t/\tau$ (equation 2.3). τ is the total computation time. Then equation 2.4 will transform to

$$\max_{0\leq s\leq 1}\frac{\left|\langle\tilde{\Phi}_1(s)|\frac{\mathrm{d}\tilde{H}(s)}{\mathrm{d}s}|\tilde{\Phi}_0(s)\rangle\right|}{\Delta E_{1,0}(s)^2}\ll\tau \tag{2.5}$$

which is an estimation of the computation time τ. It depends on the energy gap of the ground and the first excited state $\Delta E_{1,0}$. The first excited state $i = 1$ is used as it returns the lowest gap to the ground state. This is one of the most challenging problems in adiabatic quantum computing and will be described in more detail in the next section 2.3.2. [2, 24]
At this point it is necessary to note that equation 2.4 is an approximation, where some counterexamples are known e.g. [26]. More accurate approximations have been developed in recent years, one example can be found in [27].

2.3.2 Energy gap and quantum phase transitions

The energy gap between the ground and the first excited state $\Delta E_{1,0}$ has an influence on the computation time τ, hence on the performance of the annealing procedure. According to equation 2.5 the computation time τ becomes larger the smaller the gap is. Using a shorter computation time will result in a system that does not stay in its instantaneous eigenstate. This is one of the major problems in quantum annealing. [28]
To get a better understanding of the energy gap and its connection to the complexity of the problem one needs to look at quantum phase transitions. During the time evolution the system is expected to undergo such a phase transition as the annealing procedure starts in a trivial state and then transforms into a highly non-trivial one at the end of the process. Such quantum phase transitions are

known to have a vanishing energy gap in the thermodynamic limit ($N \to \infty$). [28]
There are two types of quantum phase transitions. For first order phase transitions the minimum gap $min\Delta E_{1,0}(s)$ closes exponentially with system size N, namely $min\Delta E_{1,0}(s) \propto e^{-cN}$, with $c > 0$. Second order phase transitions scale polynomially $min\Delta E_{1,0}(s) \propto N^{-l}$, with $l > 0$. Comparing this to equation 2.5 results in $\tau \propto e^{2cN}$ for first order and $\tau \propto N^{2l+1}$ for second order phase transitions (Nominator of $\mathcal{O}(N)$ can be ignored) [29]. Even though quantum phase transitions occur in the thermodynamic limit, it gives a lot of information about the complexity of the system. Optimization problems that undergo a first-order phase transition are hard to solve as the computation time τ scales exponentially with the system size N. Problems with a polynomially closing gap, hence a polynomially scaling computation time τ, are considered easy to solve. [29]
Avoiding a first-order phase transition, e.g. by an inhomogeneous transverse field, like in [30], would mean an exponential speed up. It is part of current research to weaken or avoid first-order phase transitions. Another example of this is reverse annealing, which we will discuss in the next section.

2.3.3 Reverse annealing (RA)

RA is an enhanced method of quantum annealing and was first introduced by Perdomo-Ortiz *et al* as 'sombrero adiabatic quantum computation' [18]. While QA starts in a uniform superposition of all possible states (ground state of the transverse field), RA starts in a classical state. This classical state, very often called candidate state, may be chosen by a classical method like parallel tempering. During the anneal the transverse field will get turned on and then off again. The Hamiltonian for such a schedule is described by

$$\hat{H}(t) = s_t\hat{H}_P + (1 - s_t)(1 - \lambda_t)\hat{H}_{init} + (1 - s_t)\lambda_t\hat{V}_{TF} \tag{2.6}$$

The subscript t indicates time dependence and is used for clarity. s_t and λ_t rise from 0 to 1 over the annealing process. The ground state of the Problem-Hamiltonian $\hat{H}_P$ is the desired solution. $\hat{H}_{init}$ is the initial Hamiltonian of the classical starting state e.g. $-\sum_i^N \epsilon_i\hat{\sigma}_i^z$ and V_{TF} is the transverse field $-\sum_i^N \hat{\sigma_i^x}$, N is the number of qubits. Note that $\lambda = 1$ for all t leads to the conventional QA method. [18, 19]
It is shown that a smart choice of the candidate state will yield an improved performance [18]. In a paper of Ohkuwa *et al.* the performance of reverse annealing got investigated by a mean-field theory [19].
The paper shows that if a candidate state is sufficiently close to the solution then there would be a possible way from the start to the end of the annealing procedure that is avoiding a first-order phase transition. With 'way' we mean the tuning of the parameters s and λ over time. Besides they show that if it is not possible to go around a first-order phase transition RA will weaken the effect of it. More details can be found in [19].
In a later paper it got proven that their results match with dynamical investigations. [31]

There exist several other papers for different usage of the RA method. E.g. Nicholas Chancellor describes in [21] classical state-of-the-art algorithms (Population annealing and parallel tempering) which are using RA as a local search. RA is also implemented in the D-Wave machine [32].

2.4 LHZ-model

The minimum energy gap is not the only challenge in QA. Another one in realizing quantum annealers are the interactions between qubits according to the J_{ij} matrix. As mentioned above, the optimization problems are mapped onto an Ising-model, see equation 2.2. Physical qubits interact fundamentally quasi-local by nature, therefore the control over the interactions J_{ij} is very restricted. Looking at figure 2.3 A, we see an Ising chain with interactions J. Nearest neighbor interactions like J_{12}, J_{23} and J_{34} (blue lines) are easy to implement on a quantum device. With long-range interactions like J_{24} (orange line) difficulties arise, as qubits 1 and 4 need to interact without interfering with the other qubits 2 and 3. Not being able to implement these interactions leads to a large overhead in auxiliary variables. [33]
An architecture to avoid this problem got introduced in 2015 by W. Lechner, P. Hauke and P. Zoller, therefore it is often referred to as the LHZ-model. [33]
In the LHZ-model one transforms the qubits from the Ising-model, now called logical qubits, to physical qubits. These physical qubits give information about the parity of the logical qubits. Parallel (aligned) spins represent a qubit with value 0 (1). The parity of qubit 1 to qubit 2 gives the first physical qubit and the element J_{12} is the corresponding local field. This means that the system gets enlarged to $N_p = N_l(N_l - 1)/2$ physical qubits. N_l is the number of logical qubits. This means that $N_l = 4$ logical qubits will result in $N_p = 6$ physical qubits. With the increased system size in the LHZ-model, configurations are possible which do not correspond to a state in the Ising-model. These 'unphysical' states will get an energy penalty via $N_C = N_p - N_l + 1$ constraints. This would be $N_C = 3$ constraints for $N_l = 4$. [33]
One convenient way to construct these constraints is via closed loops of logical qubits (eg. $\hat{\sigma}^z_{13}$ - $\hat{\sigma}^z_{23}$ - $\hat{\sigma}^z_{24}$ - $\hat{\sigma}^z_{14}$) which have to fullfill specific conditions. The conditions are that either none, two or all four of the physical qubits are 1. Not meeting this condition will result in a shift to higher energies. A visualization of this description can be seen in figure 2.3. Here auxillary qubits has been implemented in the bottom line to be able to treat every constraint as a 4-body plaquette. One can avoid this additional qubits by treating the bottom line as 3-body plaquettes with adjusted constraint condition. Every 3-body plaquette needs 1 or 3 qubits to be 1. [33]
Given the information above one can write down the LHZ-Hamiltonian:

$$\hat{H}_{LHZ} = \hat{H}_1 + \hat{H}_C = -\sum_{k=1}^{N_p} J_k \hat{\sigma}^z_k - \sum_{l=1}^{N_C} C_l \hat{\sigma}^z_{l,n} \hat{\sigma}^z_{l,e} \hat{\sigma}^z_{l,s} \hat{\sigma}^z_{l,w} \tag{2.7}$$

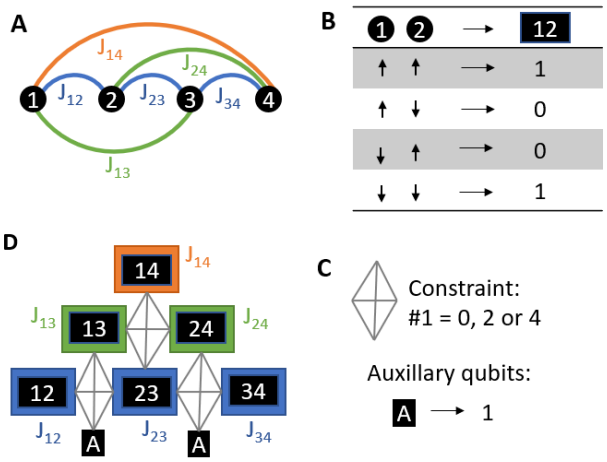

Figure 2.3: **A**: Ising chain of $N_l = 4$ spins. **B** shows the translation from logical to physical qubits. **C** specifies the constraint condition and **D** shows how the LHZ-model builds up. The constraint plaquettes consist of 4 qubits, therefore auxiliary spins get added to the bottom line. Their value is fixed to 1.

J_k is the local field for the interaction strength ($J_1 = J_{12}$ etc.) and C_l as the constraint strength. C_l is a constant which needs to be high enough to lift the unphysical states (at least) above the first excited state. N_C are the number of constraint plaquettes. The indices n, e, s and w of the constraint qubits labels the northern, southern, eastern and western qubit on plaquette l. One can distinguish two parts in the LHZ-Hamiltonian $\hat{H}_{LHZ}$: the local field Hamiltonian $\hat{H}_1$ and the constraint Hamiltonian $\hat{H}_C$. [33]
A quantum annealer based on the LHZ-model will need local fields while the constraints get mediated by nearest-neighbor interactions.
This master thesis is about how RA has been implemented in the LHZ-model.

3 Free energy and magnetization

In this chapter we will derive an equation for the magnetization. With this formula we can analyze the magnetization and any occurring phase transitions. This is done in the next chapter, section 5.1. We will follow the procedure stated in [34]. See also [35].
We set up the Hamiltonian proposed in [35] (equation 2.6) but will use the time-dependent letters A, B and C for the coefficients for simplicity. The Hamiltonian is

$$\hat{H} = A\hat{H}_{init} + B\hat{H}_p + C\hat{V}_{TF}, \tag{3.1}$$

with $\hat{H}_P$ as the LHZ-Hamiltonian $\hat{H}_{LHZ} = \hat{H}_1 + \hat{H}_C$ given in equation 2.7. The terms are

$$\hat{H}_1 = -\sum_{k=1}^{N_p} J_k \hat{\sigma}_k^z, \tag{3.2}$$

and

$$\hat{H}_C = -\sum_{l=1}^{N_C} C_l \hat{\sigma}_{l,n}^z \hat{\sigma}_{l,e}^z \hat{\sigma}_{l,s}^z \hat{\sigma}_{l,w}^z. \tag{3.3}$$

N_p is the number of physical qubits, J_k is the local field and corresponds to the interaction constants J_{ij} from the Ising-model. The sum in equation 3.3 goes over all N_C constraint plaquettes. A plaquette consists of 4 qubits, northern, eastern, southern and western qubit. C_l denotes the constraint strength.
The transverse field $\hat{V}_{TF}$ is given as

$$\hat{V}_{TF} = -\sum_{k=1}^{N_p} h_k \hat{\sigma}_k^x. \tag{3.4}$$

For the initial Hamiltonian we choose the local field term $\hat{H}_1$ of the LHZ-Hamiltonian. It is given in equation 3.2.
Now we can calculate the partition function $Z = Tr(exp(-\beta\hat{H}))$ with β as the inverse temperature. Applying the Trotter-Suzuki decomposition to separate the $\hat{\sigma}^z$ and $\hat{\sigma}^x$ terms results in

$$
\begin{aligned}
Z &= \lim_{M\to\infty} Z_M \\
&= \lim_{M\to\infty} Tr\left(\left\{\exp\left[-\frac{\beta}{M}(A\hat{H}_{init}+B\hat{H}_p)\right]\exp\left[\frac{-\beta C}{M}\hat{V}_{TF}\right]\right\}^M\right),
\end{aligned}
\tag{3.5}
$$

where M is the Trotter number. Further we rewrite the trace via an orthonormal basis $|\{\sigma^z\}\rangle$ that diagonalizes the z component of the Pauli matrices. Here $\sum_{\{\sigma^z\}}$ is the sum over all 2^{N_p} possible spin configurations and $\{\sigma^z\} = \bigotimes_{k=1}^{N_p} |\sigma_k^z\rangle$. This leads to the equation

$$
Z_M = \sum_{\{\sigma^z\}} \langle\{\sigma^z\}| \left\{\exp\left[-\frac{\beta}{M}(A\hat{H}_{init}+B\hat{H}_p)\right]\exp\left[\frac{-\beta C}{M}\hat{V}_{TF}\right]\right\}^M |\{\sigma^z\}\rangle . \tag{3.6}
$$

Now we create M replicas of the Identity matrix

$$
\mathbb{1} = \prod_{\alpha=1}^{M}\mathbb{1}(\alpha) = \prod_{\alpha=1}^{M}\sum_{\{\sigma^z(\alpha)\}} |\{\sigma^z(\alpha)\}\rangle\langle\{\sigma^z(\alpha)\}| \sum_{\{\sigma^x(\alpha)\}} |\{\sigma^x(\alpha)\}\rangle\langle\{\sigma^x(\alpha)\}| , \tag{3.7}
$$

which we insert between the $\hat{\sigma}^z$ and the $\hat{\sigma}^x$ part of the equation 3.6. This gives

$$
\begin{aligned}
Z_M &= \sum_{\{\sigma^z\}} \langle\{\sigma^z\}| \left\{\exp\left[-\frac{\beta}{M}(A\hat{H}_{init}+B\hat{H}_p)\right]\prod_{\alpha=1}^{M}\mathbb{1}(\alpha)\exp\left[\frac{-\beta C}{M}\hat{V}_{TF}\right]\right\}^M |\{\sigma^z\}\rangle \\
&= \sum_{\{\sigma^z\}} \langle\{\sigma^z\}| \left\{\prod_{\alpha=1}^{M}\sum_{\{\sigma^z(\alpha)\}}\sum_{\{\sigma^x(\alpha)\}} \exp\left[-\frac{\beta}{M}(A\hat{H}_{init}(\alpha)+B\hat{H}_p(\alpha))\right]\right. \\
&\quad \left. |\{\sigma^z(\alpha)\}\rangle\langle\{\sigma^z(\alpha)\}| |\{\sigma^x(\alpha)\}\rangle\langle\{\sigma^x(\alpha)\}| \exp\left[\frac{-\beta C}{M}\hat{V}_{TF}(\alpha)\right]\right\} |\{\sigma^z\}\rangle .
\end{aligned}
\tag{3.8}
$$

$\hat{H}_{init}$ and $\hat{H}_p$ depend on $\hat{\sigma}^z$. Acting their eigenvector $|\{\sigma^z(\alpha)\}\rangle$ on them will return the eigenvalues $\sigma^z(\alpha)$ with the corresponding eigenvectors ($\hat{\sigma}^z|\sigma^z\rangle = \sigma^z|\sigma^z\rangle$). The same thing happens with using $\hat{\sigma}^x$ to the left. As there are no operators anymore one can pull $|\{\sigma^z(\alpha)\}\rangle$ to the left and $|\{\sigma^x(\alpha)\}\rangle$ to the right. Now the equation transforms to

$$
\begin{aligned}
Z_M = \sum_{\{\sigma^z\}} \langle\{\sigma^z\}| \Bigg\{ \prod_{\alpha=1}^{M} \sum_{\{\sigma^z(\alpha)\}} \sum_{\{\sigma^x(\alpha)\}} |\{\sigma^z(\alpha)\}\rangle \\
\exp\left[\frac{\beta}{M}\left(A\sum_{k=1}^{N_p} J_k\sigma_k^z(\alpha) + B(\sum_{k=1}^{N_p} J_k\sigma_k^z(\alpha) + \sum_{l=1}^{N_C} C_l\sigma_{l,n}^z(\alpha)\sigma_{l,e}^z(\alpha)\sigma_{l,s}^z(\alpha)\sigma_{l,w}^z(\alpha))\right)\right] \\
\exp\left[\frac{\beta C}{M}\sum_{k=1}^{N_p} h_k\sigma_k^x(\alpha)\right] \langle\{\sigma^z(\alpha)\}| \, |\{\sigma^x(\alpha)\}\rangle \langle\{\sigma^x(\alpha)\}| \Bigg\} |\{\sigma^z\}\rangle \,.
\end{aligned}
\tag{3.9}
$$

In addition we write out the product over α and use $T_z(\alpha) = \frac{\beta}{M}\left(A\sum J_k\sigma_k^z(\alpha) + B(\sum J_k\sigma_k^z(\alpha) + \sum C_l\sigma_{l,n}^z(\alpha)\sigma_{l,e}^z(\alpha)\sigma_{l,s}^z(\alpha)\sigma_{l,w}^z(\alpha))\right)$ and $T_x(\alpha) = \frac{\beta C}{M}\sum h_k\sigma_k^x(\alpha)$. We receive

$$
\begin{aligned}
Z_M = \sum_{\{\sigma^z\}} \langle\{\sigma^z\}| \Bigg\{ \sum_{\{\sigma^z(1)\}} \sum_{\{\sigma^x(1)\}} |\{\sigma^z(1)\}\rangle \exp\left[T_z(1)\right] \exp\left[T_x(1)\right] \\
\langle\{\sigma^z(1)\}| \, |\{\sigma^x(1)\}\rangle \langle\{\sigma^x(1)\}| \sum_{\{\sigma^z(2)\}} \sum_{\{\sigma^x(2)\}} |\{\sigma^z(2)\}\rangle \\
\exp\left[T_z(2)\right] \exp\left[T_x(2)\right] \langle\{\sigma^z(2)\}| \, |\{\sigma^x(2)\}\rangle \langle\{\sigma^x(2)\}| \ldots \\
\sum_{\{\sigma^z(M)\}} \sum_{\{\sigma^x(M)\}} |\{\sigma^z(M)\}\rangle \exp\left[T_z(M)\right] \exp\left[T_x(M)\right] \\
\langle\{\sigma^z(M)\}| \, |\{\sigma^x(M)\}\rangle \langle\{\sigma^x(M)\}| \Bigg\} |\{\sigma^z\}\rangle \,.
\end{aligned}
\tag{3.10}
$$

Terms cancel if $\langle\{\sigma^z\}|$ and $|\{\sigma^z(1)\}\rangle$ are not equal ($\delta_{ij} = \langle i|j\rangle$). The equation reduces to

$$
\begin{aligned}
Z_M = \sum_{\{\sigma^z(1)\}} \sum_{\{\sigma^x(1)\}} \exp\left[T_z(1)\right] \exp\left[T_x(1)\right] \\
\langle\{\sigma^z(1)\}| \, |\{\sigma^x(1)\}\rangle \langle\{\sigma^x(1)\}| \sum_{\{\sigma^z(2)\}} \sum_{\{\sigma^x(2)\}} |\{\sigma^z(2)\}\rangle \\
\exp\left[T_z(2)\right] \exp\left[T_x(2)\right] \langle\{\sigma^z(2)\}| \, |\{\sigma^x(2)\}\rangle \langle\{\sigma^x(2)\}| \ldots \\
\sum_{\{\sigma^z(M)\}} \sum_{\{\sigma^x(M)\}} |\{\sigma^z(M)\}\rangle \exp\left[T_z(M)\right] exp\left[T_x(M)\right] \\
\langle\{\sigma^z(M)\}| \, |\{\sigma^x(M)\}\rangle \langle\{\sigma^x(M)\}| \, |\{\sigma^z(1)\}\rangle \,.
\end{aligned}
\tag{3.11}
$$

The formula can further be simplified by using $\prod_\alpha$ again and by introducing periodic boundary conditions so that $M + 1 = 1$. This leads to

$$
\begin{aligned}
Z_M = \sum_{\{\sigma^z(\alpha)\}} \sum_{\{\sigma^x(\alpha)\}} \prod_{\alpha=1}^{M} \exp\Big[\frac{\beta}{M}\Big(A\sum_{k=1}^{N_p} J_k\sigma_k^z(\alpha) + \\
B(\sum_{k=1}^{N_p} J_k\sigma_k^z(\alpha) + \sum_{l=1}^{N_C} C_l\sigma_{l,n}^z(\alpha)\sigma_{l,e}^z(\alpha)\sigma_{l,s}^z(\alpha)\sigma_{l,w}^z(\alpha))\Big)\Big] \exp\Big[\frac{\beta C}{M}\sum_{k=1}^{N_p} h_k\sigma_k^x(\alpha)\Big] \\
\langle\{\sigma^z(\alpha)\}||\{\sigma^x(\alpha)\}\rangle \langle\{\sigma^x(\alpha)\}||\{\sigma^z(\alpha+1)\}\rangle .
\end{aligned}
\tag{3.12}
$$

Further following [35] we use the delta distribution $f(\sum\sigma_i^z) = \int dm\ \delta(Nm - \sum\sigma_i^z)f(m)$ to rewrite the equation. The equation transforms to

$$
\begin{aligned}
Z_M = \sum_{\{\sigma^z(\alpha)\}} \sum_{\{\sigma^x(\alpha)\}} \prod_{\alpha=1}^{M} \int dm(\alpha)\ \delta\Big(N_p m(\alpha) - \sum_{k=1}^{N_p}\sigma_k^z(\alpha)\Big) \\
\exp\Big[\frac{\beta}{M}\Big(A\sum_{k=1}^{N_p} J_k\sigma_k^z(\alpha) + B\,(\sum_{k=1}^{N_p} J_k\sigma_k^z(\alpha) + \sum_{l=1}^{N_C} C_l\sigma_{l,n}^z(\alpha)\sigma_{l,e}^z(\alpha)\sigma_{l,s}^z(\alpha)\sigma_{l,w}^z(\alpha))\Big)\Big] \\
\exp\Big[\frac{\beta\ C}{M}\sum_{k=1}^{N_p} h_k\sigma_k^x\Big] \langle\{\sigma^z(\alpha)\}||\{\sigma^x(\alpha)\}\rangle \langle\{\sigma^x(\alpha)\}||\{\sigma^z(\alpha+1)\}\rangle .
\end{aligned}
\tag{3.13}
$$

Then we can use

$$
\delta\Big(N_p m - \sum_{k=1}^{N_p}\sigma_k^z\Big) = \int d\tilde{m} \exp\Big(-\tilde{m}\Big(N_p m - \sum_{k=1}^{N_p}\sigma_k^z\Big)\Big) \tag{3.14}
$$

to insert in 3.13. m is the magnetization and $\tilde{m}$ is the conjugate variable. We now receive

$$
\begin{aligned}
Z_M = \sum_{\{\sigma^z(\alpha)\}} \sum_{\{\sigma^x(\alpha)\}} \prod_{\alpha=1}^{M} \iint dm(\alpha)\ d\tilde{m}(\alpha) \exp\Big[-\tilde{m}(\alpha)\Big(N_p m(\alpha) - \sum_{k=1}^{N_p}\sigma_k^z(\alpha)\Big)\Big] \\
\exp\Big[\frac{\beta}{M}\Big((A+B)\sum_{k=1}^{N_p} J_k\sigma_k^z(\alpha) + B\sum_{l=1}^{N_C} C_l\sigma_{l,n}^z(\alpha)\sigma_{l,e}^z(\alpha)\sigma_{l,s}^z(\alpha)\sigma_{l,w}^z(\alpha)\Big)\Big] \\
\exp\Big[\frac{\beta C}{M}\sum_{k=1}^{N_p} h_k\sigma_k^x(\alpha)\Big] \langle\{\sigma^z(\alpha)\}||\{\sigma^x(\alpha)\}\rangle \langle\{\sigma^x(\alpha)\}||\{\sigma^z(\alpha+1)\}\rangle .
\end{aligned}
\tag{3.15}
$$

We can rewrite the constraint term $\sum_{l=1}^{N_C} C_l\sigma_{l,n}^z\sigma_{l,e}^z\sigma_{l,s}^z\sigma_{l,w}^z$ following [36]. In this paper they derive an expression for the energy expressed as a function of the number of qubits in the 4- (n_4) and 3-body (n_3) plaquettes, which is

$$\begin{aligned} E_{N_p}(m) &= -C_l(n_4 m^4 + n_3 m^3) \\ &= -C_l\left(N_p - \sqrt{1+8N_p} + 2\right)m^4 - C_l\left(\sqrt{0.25+2N_p} - 1.5\right)m^3. \end{aligned} \tag{3.16}$$

Here C_l is the constraint strength.
Inserting 3.16 in 3.15 and using $\langle\{\sigma_z\}|\,|\{\sigma_x\}\rangle = \prod_{k=1}^{N_p}\langle\sigma_k^z|\sigma_k^x\rangle$ gives

$$\begin{aligned} Z_M = \sum_{\{\sigma^z(\alpha)\}}\sum_{\{\sigma^x(\alpha)\}}\prod_{\alpha=1}^{M}\iint dm(\alpha)\, d\tilde{m}(\alpha)\exp\Big[&- N_p\tilde{m}(\alpha)m(\alpha) + \\ \frac{\beta B C_l}{M}(n_4 m^4(\alpha) + n_3 m^3(\alpha))\Big]\exp\Bigg[\sum_{k=1}^{N_p}\Bigg(&\left((A+B)\frac{\beta}{M}J_k + \tilde{m}\right)\sigma_k^z(\alpha) + \\ \frac{\beta C}{M}h_k\sigma_k^x(\alpha)\Bigg)\Bigg]\prod_{k=1}^{N_p}&\langle\sigma_k^z(\alpha)|\,|\sigma_k^x(\alpha)\rangle\,\langle\sigma_k^x(\alpha)|\sigma_k^z(\alpha+1)\rangle\,. \end{aligned} \tag{3.17}$$

Now we rewrite the sums $\sum_{\{\sigma^z(\alpha)\}}\sum_{\{\sigma^x(\alpha)\}} = \prod_{k=1}^{N_p}\sum_{\sigma_k^z(\alpha)}\sum_{\sigma_k^x(\alpha)}$ and pull out the sum out of the second exponential to obtain

$$\begin{aligned} Z_M = \prod_{k=1}^{N_p}\sum_{\sigma_k^z(\alpha)}\sum_{\sigma_k^x(\alpha)}\iint\prod_{\alpha=1}^{M}dm(\alpha)\, d\tilde{m}(\alpha)\exp\Bigg[\sum_{\alpha=1}^{M}\Big(&- N_p\tilde{m}(\alpha)m(\alpha) + \\ \frac{\beta B C_l}{M}(n_4 m^4(\alpha) + n_3 m^3(\alpha))\Big)\Bigg]\prod_{\alpha=1}^{M}\prod_{k=1}^{N_p}\exp\Bigg[&\left((A+B)\frac{\beta}{M}J_k + \tilde{m}\right)\sigma_k^z(\alpha) + \\ \frac{\beta C}{M}h_k\sigma_k^x(\alpha)\Bigg]\prod_{k=1}^{N_p}&\langle\sigma_k^z(\alpha)|\,|\sigma_k^x(\alpha)\rangle\,\langle\sigma_k^x(\alpha)|\sigma_k^z(\alpha+1)\rangle\,. \end{aligned} \tag{3.18}$$

We can cancel the other products over k before the steps get reversed. Letting the vectors act to the exponential again will transform them back to operators. With $Z_k = (A+B)\frac{\beta}{M}J_k + \tilde{m}$, $X_k = \frac{\beta C}{M}h_k$ and
$K_{\tilde{m}} = \exp\left[\sum_\alpha\left(-N_p\tilde{m}(\alpha)m(\alpha) + \frac{\beta B C_l}{M}(n_4 m^4(\alpha) + n_3 m^3(\alpha))\right)\right]$ we receive

$$\begin{aligned} Z_M = \prod_{k=1}^{N_p}\sum_{\sigma_k^z(\alpha)}\sum_{\sigma_k^x(\alpha)}\iint\prod_{\alpha=1}^{M}dm(\alpha)\, d\tilde{m}(\alpha)K_{\tilde{m}}\prod_{\alpha=1}^{M}&\langle\sigma_k^z(\alpha)|\exp\left[Z_k\hat{\sigma}_k^z(\alpha)\right] \\ |\sigma_k^x(\alpha)\rangle\,\langle\sigma_k^x(\alpha)|\exp&\left[X_k(k)\hat{\sigma}_k^x(\alpha)\right]|\sigma_k^z(\alpha+1)\rangle\,. \end{aligned} \tag{3.19}$$

After executing the product over α the partition function writes as

$$
\begin{aligned}
Z_M = \prod_{k=1}^{N_p} \sum_{\sigma_k^z(1)} \sum_{\sigma_k^x(1)} \sum_{\sigma_k^z(2)} \sum_{\sigma_k^x(2)} \dots \sum_{\sigma_k^z(M)} \sum_{\sigma_k^x(M)} \iint \prod_{\alpha=1}^{M} \Big(dm(\alpha)\, d\tilde{m}(\alpha) \Big) K_{\tilde{m}} \\
\langle \sigma_k^z(1)| \exp\Big[Z_k \hat{\sigma}_k^z(1) \Big] |\sigma_k^x(1)\rangle \langle \sigma_k^x(1)| \exp\Big[X_k \hat{\sigma}_k^x(1) \Big] |\sigma_k^z(2)\rangle \\
\langle \sigma_k^z(2)| \exp\Big[Z_k \hat{\sigma}_k^z(2) \Big] |\sigma_k^x(2)\rangle \langle \sigma_k^x(2)| \exp\Big[X_k \hat{\sigma}_k^x(2) \Big] |\sigma_k^z(3)\rangle \dots \\
\langle \sigma_k^z(M)| \exp\Big[Z_k \hat{\sigma}_k^z(M) \Big] |\sigma_k^x(M)\rangle \langle \sigma_k^x(M)| \exp\Big[X_k \hat{\sigma}_k^x(M) \Big] |\sigma_k^z(1)\rangle \,.
\end{aligned}
\tag{3.20}
$$

With $\sum_{\sigma_k^x(1)} |\sigma_k^x(1)\rangle \langle \sigma_k^x(1)| = \mathbb{1}$ we can see that all the bras and kets cancel except the outer ones. Thus we have

$$
\begin{aligned}
Z_M = \iint \prod_{\alpha=1}^{M} \Big(dm(\alpha)\, d\tilde{m}(\alpha) \Big) \exp\Bigg[\sum_{\alpha=1}^{M} \Big(- N_p \tilde{m}(\alpha) m(\alpha) + \frac{\beta B C_l}{M} (n_4 m^4(\alpha) + \\
n_3 m^3(\alpha)) \Big) \Bigg] \prod_{k=1}^{N_p} tr\Bigg(\prod_{\alpha=1}^{M} \exp\Big[\Big((A+B) \frac{\beta}{M} J_k + \tilde{m} \Big) \hat{\sigma}^z(\alpha) \Big] \exp\Big[\frac{\beta C}{M} h_k \hat{\sigma}^x(\alpha) \Big] \Bigg).
\end{aligned}
\tag{3.21}
$$

Further, we rewrite the equation to derive a term for the free energy f

$$
\begin{aligned}
Z_M = \iint \prod_{\alpha=1}^{M} \Big(dm(\alpha)\, d\tilde{m}(\alpha) \Big) \exp\Bigg[\sum_{\alpha=1}^{M} \Big(- N_p \tilde{m}(\alpha) m(\alpha) + \frac{\beta B C_l}{M} (n_4 m^4(\alpha) + \\
n_3 m^3(\alpha)) \Big) \Bigg] \exp\Bigg[\sum_{k=1}^{N_p} \ln tr\Bigg(\prod_{\alpha=1}^{M} \exp\Big[\Big((A+B) \frac{\beta}{M} J_k + \tilde{m} \Big) \hat{\sigma}^z(\alpha) \Big] \\
\exp\Big[\frac{\beta C}{M} h_k \hat{\sigma}^x(\alpha) \Big] \Bigg) \Bigg] = \iint \prod_{\alpha=1}^{M} dm(\alpha)\, d\tilde{m}(\alpha) \exp\Big[- N_p \beta f_{N_p,M} \Big].
\end{aligned}
\tag{3.22}
$$

Thus the free energy $f_{N_p,M}$ is

$$
\begin{aligned}
f_{N_p,M} = \sum_{\alpha=1}^{M} \Big(\frac{1}{\beta} \tilde{m}(\alpha) m(\alpha) - \frac{B C_l}{N_p M} (n_4 m^4(\alpha) + n_3 m^3(\alpha)) \Big) - \\
\frac{1}{N_p \beta} \sum_{k=1}^{N_p} \ln tr\Bigg(\prod_{\alpha=1}^{M} \exp\Big[\Big((A+B) \frac{\beta}{M} J_k + \tilde{m} \Big) \hat{\sigma}^z(\alpha) \Big] \exp\Big[\frac{\beta C}{M} h_k \hat{\sigma}^x(\alpha) \Big] \Bigg).
\end{aligned}
\tag{3.23}
$$

With the solution to $\partial f_{N_p,M} / \partial m = 0$ (saddle point condition) we can derive an expression for $\tilde{m}$ that minimizes the free energy $f_{N_p,M}$ with respect to m. We receive

$$\frac{\partial f}{\partial m} = \frac{1}{\beta}\tilde{m} - \frac{B}{N_p M}(4n_4 m^3 + 3n_3 m^2) = 0, \tag{3.24}$$

which leads to

$$\tilde{m} = \frac{\beta B}{N_p M}(4n_4 m^3 + 3n_3 m^2). \tag{3.25}$$

Inserting this expression for $\tilde{m}$ in equation 3.23 gives

$$\begin{aligned} f_{N_p,M} = &\sum_{\alpha=1}^{M} \frac{BC_l}{N_p M}(3n_4 m^4(\alpha) + 2n_3 m^3(\alpha)) - \\ &\frac{1}{N_p \beta}\sum_{k=1}^{N_p} \ln tr\Bigg(\prod_{\alpha=1}^{M} \exp\Bigg[\Bigg((A+B)\frac{\beta}{M}J_k + \\ &\frac{\beta B C_l}{N_p M}(4n_4 m^3(\alpha) + 3n_3 m^2(\alpha))\Bigg)\hat{\sigma}^z(\alpha)\Bigg] \exp\left[\frac{\beta C}{M}h_k \hat{\sigma}^x(\alpha)\right]\Bigg). \end{aligned} \tag{3.26}$$

Applying the static approximation $m(\alpha) = m$ for all α to equation 3.26 results in

$$\begin{aligned} f_{N_p,M} = \frac{BC_l}{N_p}(3n_4 m^4 + 2n_3 m^3) - \frac{1}{N_p \beta}\sum_{k=1}^{N_p} \ln tr\Bigg(\exp\Bigg[\frac{\beta}{M}\Bigg(AJ_k + BJ_k + \\ \frac{BC_l}{N_p}(4n_4 m^3 + 3n_3 m^2)\Bigg)\hat{\sigma}^z\Bigg] \exp\left[\frac{\beta C}{M}h_k \hat{\sigma}^x\right]\Bigg)^M. \end{aligned} \tag{3.27}$$

Taking the reverse Suzuki-Trotter decomposition operation will delete the rest of the $M's$. This transforms the equation to

$$\begin{aligned} f_{N_p} = &\frac{BC_l}{N_p}(3n_4 m^4 + 2n_3 m^3) - \\ &\frac{1}{N_p \beta}\sum_{k=1}^{N_p} \ln tr\Bigg(\exp\left[\beta\left(AJ_k + BJ_k + \frac{BC_l}{N_p}(4n_4 m^3 + 3n_3 m^2)\right)\hat{\sigma}^z + \beta C h_k \hat{\sigma}^x\right]\Bigg). \end{aligned} \tag{3.28}$$

With the Laurent series it is possible to solve the matrix exponential of a 2x2 matrix. The free energy f_{N_p} can now be expressed as

$$f_{N_p} = \frac{BC_l}{N_p}(3n_4m^4 + 2n_3m^3) - \frac{1}{N_p\beta}\sum_{k=1}^{N_p} \ln\left[2\cosh\left(\beta\sqrt{\left(AJ_k + BJ_k + \frac{BC_l}{N_p}(4n_4m^3 + 3n_3m^2)\right)^2 + \left(Ch_k\right)^2}\right)\right]. \tag{3.29}$$

Now we insert the expressions of the number of three $n_3 = \sqrt{0.25 + 2N_p} - 1.5$ and four body plaquettes $n_4 = N_p - \sqrt{1 + 8N_p} + 2$, which gives us

$$\begin{aligned} f_{N_p} = {} & BC_l\left(\left(3 - \frac{\sqrt{9 + 72N_p} + 6}{N_p}\right)m^4 + \left(\frac{\sqrt{1 + 8N_p} - 3}{N_p}\right)m^3\right) - \\ & \frac{1}{N_p\beta}\sum_{k=1}^{N_p} \ln\left[2\cosh\left(\beta\left\{\left(AJ_k + BJ_k + BC_l(4 - \frac{\sqrt{16 + 128N_p} + 8}{N_p})m^3\right.\right.\right. \\ & \left.\left.\left. + BC_l\frac{\sqrt{2.25 + 18N_p} - 4.5}{N_p}m^2\right)^2 + \left(Ch_k\right)^2\right)\right\}^{\frac{1}{2}}\right]. \end{aligned} \tag{3.30}$$

Looking at the term $\frac{1}{\beta}\ln(2\cosh(\beta x))$ and letting $\beta \to \infty$ returns $\lim_{\beta\to\infty}\frac{1}{\beta}\ln(\exp(\beta x) + \exp(-\beta x)) = x$. Using this for 3.30 leads to

$$\begin{aligned} f_{N_p} = {} & BC_l\left(\left(3 - \frac{\sqrt{9 + 72N_p} + 6}{N_p}\right)m^4 + \left(\frac{\sqrt{1 + 8N_p} - 3}{N_p}\right)m^3\right) - \\ & \frac{1}{N_p}\sum_{k=1}^{N_p}\left\{\left(AJ_k + BJ_k + BC_l(4 - \frac{\sqrt{16 + 128N_p} + 8}{N_p})m^3\right.\right. \\ & \left.\left. + BC_l\frac{\sqrt{2.25 + 18N_p} - 4.5}{N_p}m^2\right)^2 + \left(Ch_k\right)^2\right\}^{\frac{1}{2}}. \end{aligned} \tag{3.31}$$

In the thermodynamic limit $N_p \to \infty$ the 3-body terms m^3 vanish (you can find more details in [36]). We also assume $J_k = J$ and $h_k = h$. We receive

$$f = 3BC_lm^4 - \left\{\left(AJ + BJ + 4BC_lm^3\right)^2 + \left(Ch\right)^2\right\}^{\frac{1}{2}}. \tag{3.32}$$

To derive the self consistency equation for the magnetization we need to perform $\frac{\partial f}{\partial m} = 0$. We get

$$m = \frac{AJ + BJ + 4BC_l m^3}{\sqrt{(AJ + BJ + 4BC_l m^3)^2 + (Ch)^2}}. \tag{3.33}$$

Furthermore we can modify it with a given constant c denoting the fraction of positive J values. With $c = 1$ (all J are positive) we receive the previous equation. The new equation is

$$\begin{aligned} m = c\frac{AJ + BJ + 4BC_l m^3}{\sqrt{(AJ + BJ + 4BC_l m^3)^2 + (Ch)^2}} \\ + (1 - c)\frac{-AJ - BJ + 4BC_l m^3}{\sqrt{(-AJ - BJ + 4BC_l m^3)^2 + (Ch)^2}}. \end{aligned} \tag{3.34}$$

4 RA in the LHZ-model

In this chapter we want to set up the Hamiltonian for the RA-procedure in the LHZ-model and explain the set-up for the simulation. Furthermore we go into more detail about the simulated cases to better understand the outcome.

4.1 Hamiltonian

The general RA Hamiltonian is stated in equation 2.6 and the implementation on the LHZ-model is already given in chapter 3, equation 3.1. $\hat{H}_p$ will be the the LHZ-Hamiltonian from equation 2.7 with $\hat{H}_{LHZ} = \hat{H}_1 + \hat{H}_C$. The initial Hamiltonian $\hat{H}_{init}$ will be the local field term $\hat{H}_1$. The starting state is the ground state of this Hamiltonian.
Now we write down the full Hamiltonian with specified coefficients for reverse annealing (RA) $\hat{H}_{RA}$ and conventional quantum annealing (QA) $\hat{H}_{QA}$:

$$\hat{H}_{RA} = (1 - s_t)(1 - \lambda_t)\hat{H}_1 + s_t(\hat{H}_1 + \hat{H}_C) + (1 - s_t)\lambda_t\Gamma\hat{V}_{TF} \tag{4.1}$$

$$\hat{H}_{QA} = (1 - s_t)\hat{V}_{TF} + s_t(\hat{H}_1 + \hat{H}_C) \tag{4.2}$$

with the Hamiltonian $\hat{H}_1$ and $\hat{H}_C$ given in equation 3.2 and 3.3. For the transverse field $\hat{V}_{TF}$ in equation 3.4 we set $h_k = 1$. N_p is the number of physical qubits. Γ in equation 4.1 is an additional parameter to tune the strength of the transverse field, s_t and λ_t are time-dependent and raise linearly from 0 to 1. The dependence of the coefficients of the Hamiltonian terms $\hat{H}_1$, $\hat{H}_C$, and $\hat{V}_{TF}$ can be seen in figure 4.1. The QA schedule, seen in 4.1a, consists of 2 Hamiltonians. In the start the transverse field $\hat{V}_TF$ is on and then decreases linearly till it is off at time $t = \tau$. τ is the total computation time, so $\tau = max(t)$. The problem Hamiltonian $\hat{H}_P = \hat{H}_1 + \hat{H}_C$ is 0 at $t = 0$ and raises linearly over the annealing process. The schedule for $\hat{H}_P$ does not change for RA. The difference lays in the transverse field $\hat{V}_{TF}$ and the additional initial Hamiltonian $\hat{H}_{init} = \hat{H}_1$. As the coefficient for $\hat{H}_1$ is $(1 - s_t)(1 - \lambda_t)$ the initial Hamiltonian decreases quadratically. The coefficient for $\hat{V}_{TF}$ is $(1 - s_t)\lambda_t\Gamma$ which is a parabola with (0 at $t = 0$ and $t = \tau$) a maximum at $\tau/2$.

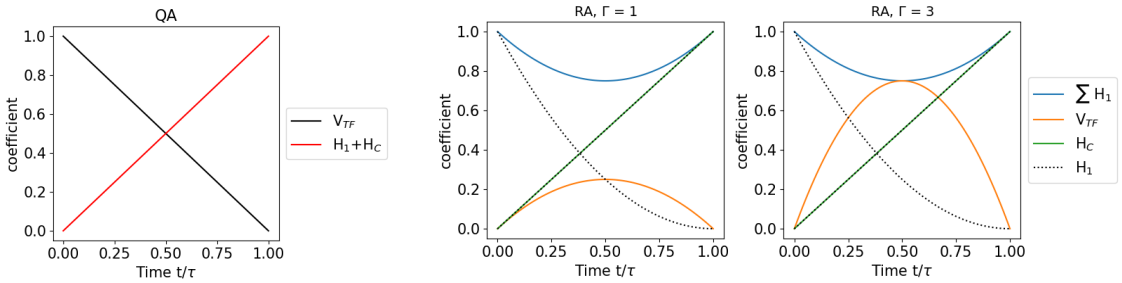

(a) QA schedule

(b) RA schedule with Γ = 1 (left) and Γ = 3 (right)

Figure 4.1: Time dependency of the coefficients of the Hamiltonian terms. The conventional QA method, seen in (a), starts at time $t = 0$ with the transverse field V_{TF}, which gets turned off linearly over time. At the end of the anneal $t = \tau$, it is 0. The problem Hamiltonian $H_{LHZ} = H_1 + H_C$ starts at 0 and grows linearly till it is fully turned on. In RA s and λ will also raise linearly from 0 to 1. This means RA, (b), starts with $\hat{H}_1$. The transverse field V_{TF} is 0 in the beginning and at the end of the anneal. The maximum strength at $\frac{\tau}{2}$ depends on Γ. The coefficients of the two $\hat{H}_1$ Hamiltonians in the equation sum up to the blue line.

4.2 Units

In QA it is common to use reduced units with $\hbar = 1$. This means that the Energy $E = \hbar\omega$ is given in [Hz]. This further implies that the J matrix values are in [Hz] as well. We will now introduce $[J_{ij}]$ as the new unit. This means that the time is given in terms of $\frac{1}{[J_{ij}]}$. If $1[J_{ij}] = 1$ [GHz] the time scales respectively to $1\tau = 1$ [ns].

4.3 Set-Up for simulation

For the simulation we set-up the Hamiltonians and the starting state and let it evolve according to the Schrödinger-equation. This is done in Phyton using the library QuTiP [37, 38].
Simulations with different computations times τ will be made for both QA and RA. This means we run the annealing schedules shown in figure 4.1 for different time lengths. The number of logical qubits N_l will be 4, this means we have $N_p = 6$ physical qubits in our systems. Furthermore we assume problems with zero magnetic field $b_i = 0$ in the Ising-Hamiltonian (equation 2.2). The constraint strength C_l is set to 5. Starting with 4 simple cases we will also run 120 samples of random J matrices with values between -1 and 1. They are discussed in the following subsections. Keep in mind that the ground state of $\hat{H}_1$ is the starting state for the RA procedure in LHZ. We also like to keep the Ising notation J_{ij} for the J matrix values.

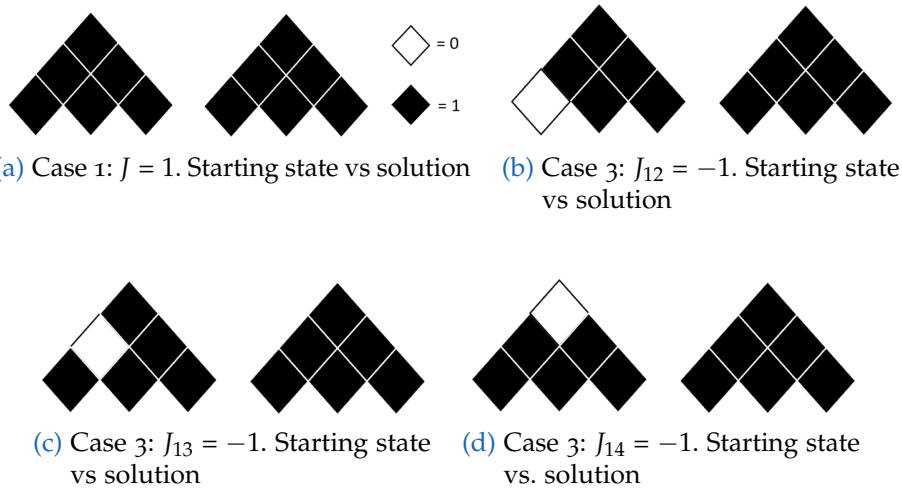

(a) Case 1: $J = 1$. Starting state vs solution

(b) Case 3: $J_{12} = -1$. Starting state vs solution

(c) Case 3: $J_{13} = -1$. Starting state vs solution

(d) Case 3: $J_{14} = -1$. Starting state vs. solution

Figure 4.2: Starting and solution states for the cases 1 and 3 on the LHZ-model with $N_p = 6$. The left figure in each subplot shows the starting state (ground state of $\hat{H}_1$) and the right figure the desired solution of the problem (groundstate of $\hat{H}_1 + \hat{H}_C$). A black (white) square is a qubit with value 1 (0). Case 1 ($J = 1$) is visualized in (a) Case 3: In (b), (c) and (d) we see 3 of the 6 possible configurations with one inverted J_{ij} element. One qubit needs to flip in each process to reach the desired state.

4.3.1 Case 1

In the first case we set all interactions to 1, so $J_{ij} = J = 1$. Looking at the Ising-model 2.2 we can see that a configuration of all spins down or up will lead to the lowest energy states. In the LHZ-model 2.7 the first part of the equation, $\hat{H}_1$, is minimized if all values are 1. This configuration does not violate any constraints. No qubits need to flip during the annealing process! This is visualized in figure 4.2a.
We have two degenerate ground states in the Ising-model 2.2 and one ground state for the LHZ-model 2.7.

4.3.2 Case 2

Here we have $J_{ij} = J = -1$. To minimize the equation for the Ising-model 2.2 there has to be an equal amount of up and down spins. For $\hat{H}_1$ in the LHZ-model 2.7 a configuration of all values 0 will return the lowest energy. This is our starting state.
The ground state of the constraint term $\hat{H}_C$ is any state which does not violate the constraint condition. This means that the ground state of $\hat{H}_1 + \hat{H}_C$ is a state, closest to the ground state of $\hat{H}_1$ which fulfills the constraint condition. This means we need to flip as few qubits as possible to obtain the lowest energy state. For $N_p = 6$ this means 2 qubits need to adjust during the annealing procedure This is visualized in figure 4.3a and 4.3b.

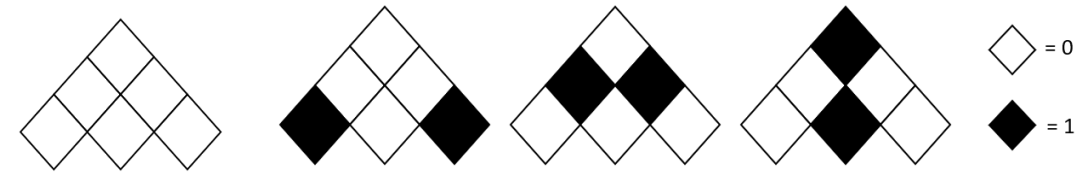

(a) Case 2: Starting state

(b) Case 2: Solution

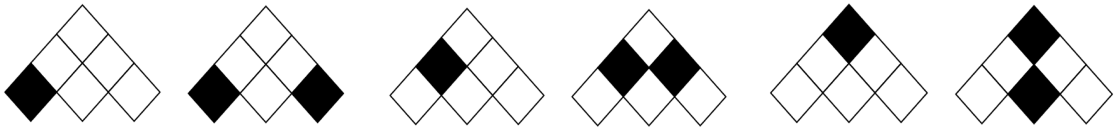

(c) Case 4: $J_{12} = -1$. Starting state vs solution

(d) Case 4: $J_{13} = 1$. Starting state vs solution

(e) Case 4: $J_{14} = 1$. Starting state vs solution

Figure 4.3: Starting and solution states for the cases 1 and 3 on the LHZ-model with $N_p = 6$. A black (white) square is a qubit with value 1 (0). The starting state of Case 2 (groundstate of $\hat{H}_1$ with $J = -1$) is shown in (a). The corresponding solution in (b) is 3-fold degenerated. Start- and solution state of 3 of the 6 possible configurations of case 3 can be found in (b), (c) and (d). The left (right) figure in each subplot is the starting (solution) state. One qubit needs to flip in each process to reach the desired state.

In the Ising-model 2.2 we have now $\binom{N_l}{N_l/2} = 6$ degenerated ground states and half of it in the LHZ-model 2.7.

4.3.3 Case 3

In case 3 all J values in the matrix are set to 1 except one which has the value -1. As we have 6 physical qubits there are 6 possible positions to set the inverted J. Imagine an example in the Ising-model: $J_{12} = -1$ and the rest of the interactions is 1. While J_{12} prefers opposite spin direction for qubit 1 and 2 there are J_{13},J_{14} and J_{23},J_{24} which prefer aligned qubits. We can conclude that the ground state in LHZ is again all qubits 1 although the ground state energy is higher than in case 1. We note that 1 qubit has to flip to reach the solution. 3 examples are given in figure 4.2b, 4.2c and 4.2d.

4.3.4 Case 4

Here we set one element in the J_{ij} matrix to 1 and the rest to -1. In Case 2 we have 3 degenerated ground states. One of those states is the ground state in this case, depending on which element of the J_{ij} matrix is set to 1. The ground state for $\hat{H}_1$ will have a value 1 on the site where we set $J = 1$. This is shown in the left picture of the subfigures 4.3c, 4.3d and 4.3e. The right pictures of these subfigures show the solution state. Depending on which J_{ij} has been inverted, the solution state matches with one of the degenerated groundstates of case 2, figure 4.3b. Similar to Case 3, 1 qubit has to flip to reach the desired solution.

5 Results

This chapter lists the results from simulation and analytics. In the first section we use the performed analysis from chapter 3 to obtain the magnetization for QA and RA in LHZ. In the second section we show the resulting fidelities of our simulations of the 4 previously discussed cases and 120 runs of random J-matrices. The third and last section is about the variance of energy and how it can help to better understand the obtained results.

5.1 Magnetization

In chapter 3 we received an expression for the magnetization, see equation 3.34. In section 4.1 we specified the coefficients A, B and C in equation 4.1. We also keep $h = 1$ and $\Gamma = 1$. The coefficients are

$$A = (1 - s_t)(1 - \lambda_t), \tag{5.1}$$

$$B = s_t, \tag{5.2}$$

$$C = (1 - s_t)\lambda_t\Gamma. \tag{5.3}$$

In figure 5.1 we see the magnetization plotted for every value of s and λ for different cases of c. $c = 0$ ($c = 1$) corresponds to $J = -1$ ($J = 1$) for all places ij. These cases are seen in figures 5.1a and 5.1d. 5.1a, $J = -1$, is the inverted picture of 5.1d, $J = 1$.
The way for QA over this magnetization landscape goes over a fixed $\lambda = 1$ from $s = 0$ to $s = 1$. RA starts at $s = \lambda = 0$ and end at $s = \lambda = 1$. There is no fixed way RA has to go between the starting and the end point.
For $J = -1$ and $J = 1$, RA does not change magnetization, independent of the way it takes to the endpoint, whereas QA can not avoid a jump in magnetization. This is different if $c = 0.6$. $c = 0.6$ means that 60% are $J = 1$ and 40% are $J = -1$. In figure 5.1b we do not observe a sudden change of magnetization for QA. RA shows the behaviour as before.
In figure 5.1c we see the magnetization landscape for $c = 0.7$. Here QA and RA experience a jump in magnetization and there is no way for RA to avoid it. The jump for RA looks smaller than the one for QA, but for better comparison we need to look at the actual values. They are plotted in figure 5.2.
For $c = 0$ and $c = 1$ in figure 5.2a and 5.2d we see the behaviour already examined in the figures in 5.1a and 5.1d. The way for RA is chosen to be $s = \lambda$ as in the schedule in figure 4.1b. There is a jump in magnetization for QA which

corresponds to a first-order phase transition. This is related to an exponential gap closing, described in section 2.3.2, which is a major challenge in QA. In this difficult region it is necessary to go slow to stay in the instantaneous ground state.

For $c = 0.6$ in figure 5.2b we see a smooth change of magnetization for QA which corresponds to figure 5.1b. Figure 5.2c with $c = 0.7$ proofs that the jump in magnetization for RA is smaller than the one for QA.

The jump in magnetization can be related to an instant change of the configuration. The magnetization and therefore the state before the jump is significantly different from the one after the jump. We can see the jump as a proxy for the distance between the two states. The tunneling rate depends on the distance between two local minima, therefore a smaller jump means a higher tunneling rate. This would lead to a better performance of RA for $c = 0.7$.

To understand why we do not see any change in magnetization for RA in $c = 0$

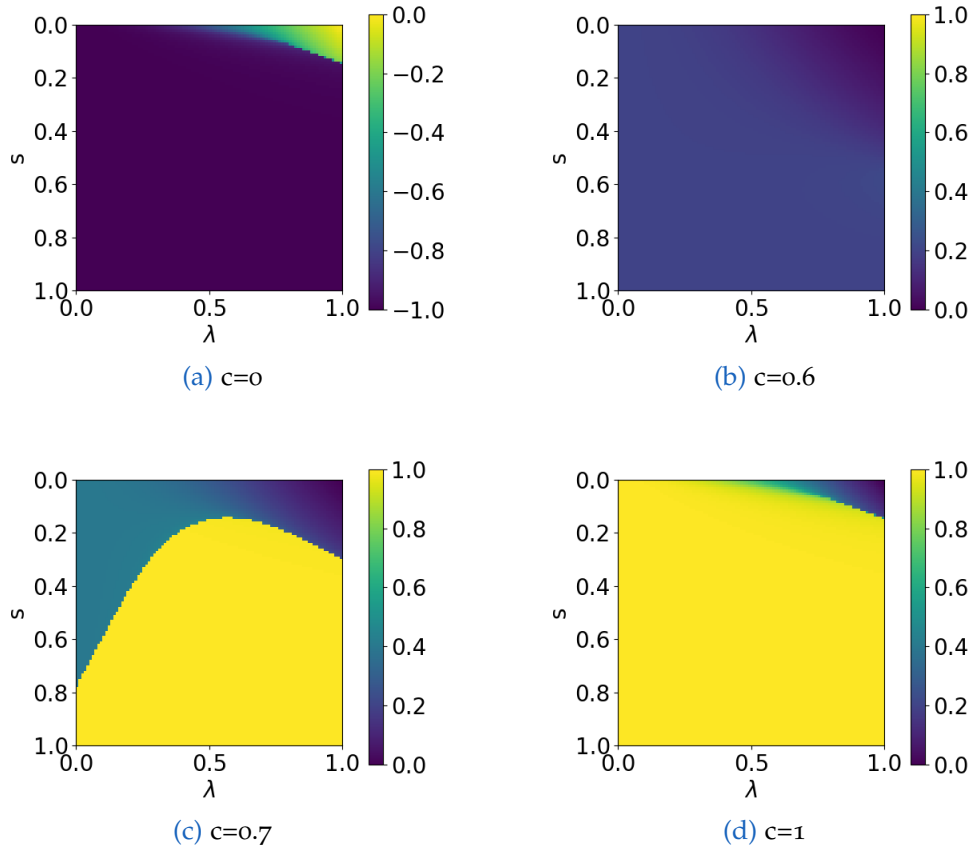

(a) c=0 (b) c=0.6

(c) c=0.7 (d) c=1

Figure 5.1: Magnetization over all values of s and λ for different fractions c of $J = 1$. QA starts at $s = 0$ and ends at $s = 1$, λ fixed to 1. RA starts at $s = \lambda = 0$ and ends at $s = \lambda = 1$. $c = 0$ in (a) shows the magnetization landscape for $J = -1$ for all qubits. QA will experience a sudden change in magnetization at s 0.2. There is no way to avoid it. RA can reach the end point of the annealing procedure without a change in magnetization. The same hold for $c = 1$ in (d) (all $J = 1$). (b) and (c) are intermediate cases with 60% and 70% of $J = 1$, the rest is $J = -1$. For (b) there is again no change for RA, but also a very weak transition for QA. In (c) there is a unavoidable jump in magnetization for both QA and RA.

(case 2, $J = -1$) we refer to the previous chapter, section 4.3.1 for case 1 ($c = 1$) and 4.3.2 for case 2 ($c = 0$). In case 1 ($c = 1$) the starting state is already the solution. The state does not need to change, therefore the magnetization does not change either. Case 2 ($c = 0$) is different. The starting state violates the constraint condition. This means that as few qubits as possible need to flip to satisfy it. For $N_p = 6$ 2 qubits need to flip. The investigated situation in figure 5.2a is based on $N \to \infty$. The system size is so big that the constraint adjusting qubit flips do not change the magnetization and therefore the state significantly. In summary, we would expect better performance for RA in both cases.
For $c = 0.6$ (figure 5.2b) we have no information about the starting and the solution state. RA starts closer to the solution state than QA, but the change in QA happens smoothly and not in a jump as in $c = 0$. Based on this statements we assume that QA for $c = 0.6$ shows better performance than QA for $c = 0$.
The jump in magnetization in $c = 0.7$ is smaller for RA than for QA, therefore we also expect better performance for RA.
The good result for RA is based on the fact that we already but information about the problem in our system, as we start with the ground state of the local field term $\hat{H}_1$. The constraint term $\hat{H}_C$ gives the remaining information in the

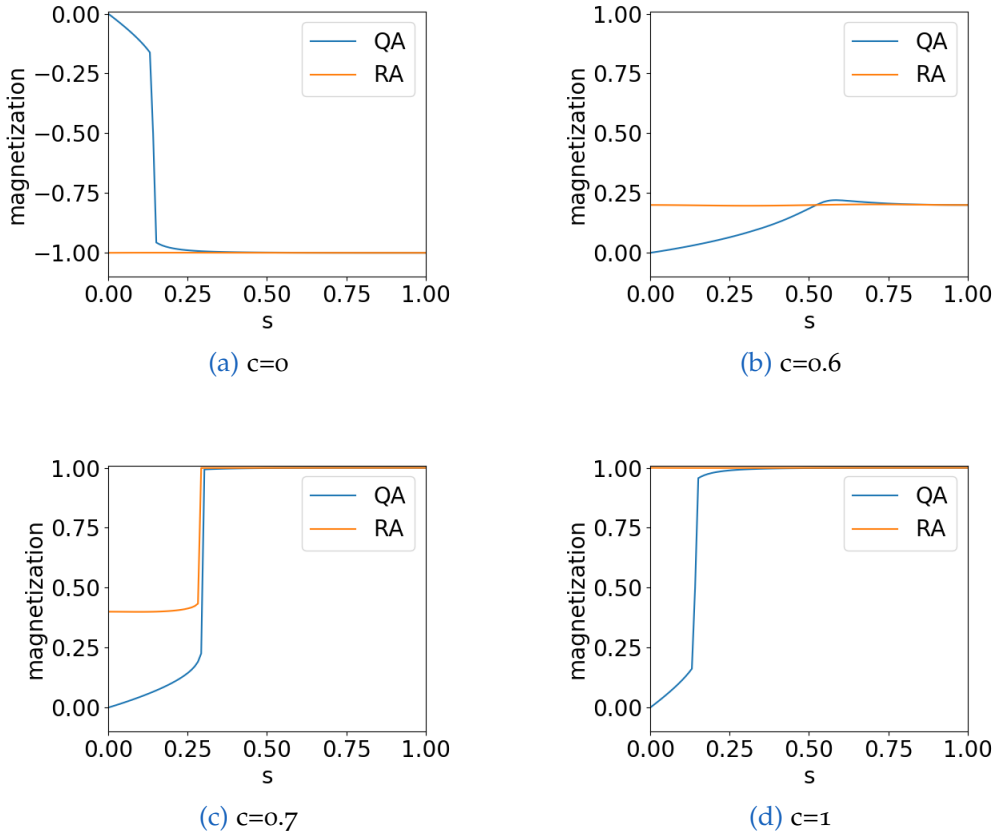

(a) c=0 (b) c=0.6

(c) c=0.7 (d) c=1

Figure 5.2: Magnetization for QA and RA over different values of s. For QA λ is fixed to 1. For RA we choose the way $s = \lambda$. This schedule is also plotted in figure 4.1b. Here the strength of the transverse field is set to $\Gamma = 1$. The same c values as in figure 5.1 are used.

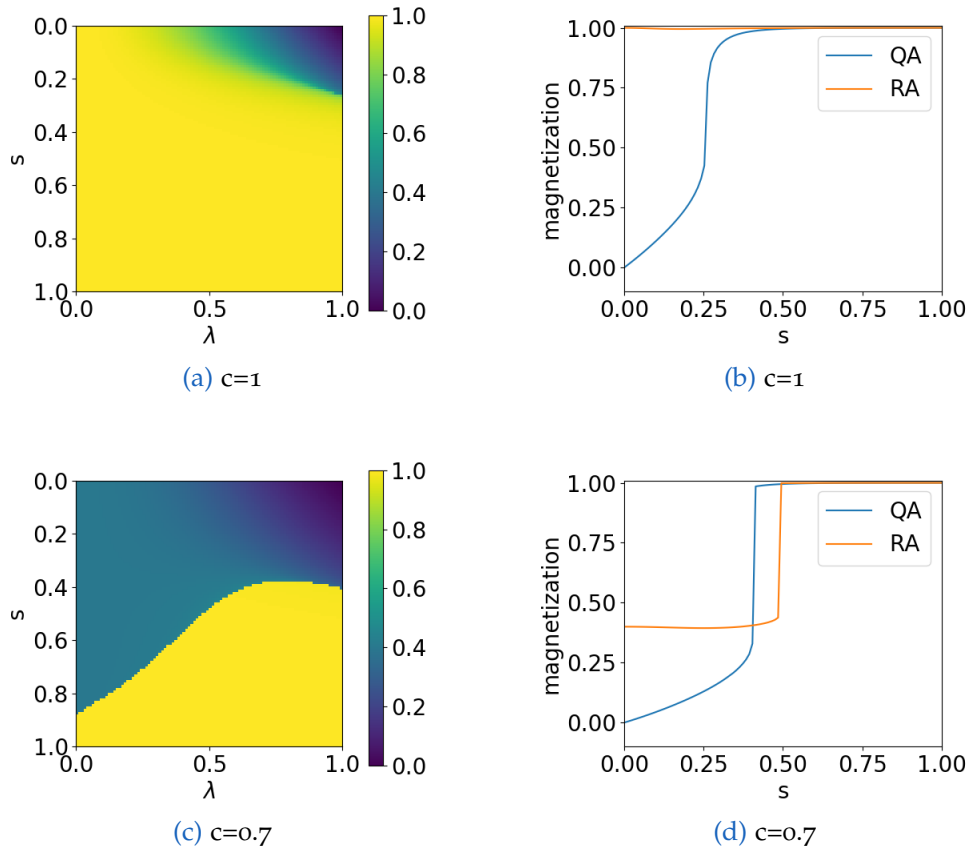

(a) c=1 (b) c=1

(c) c=0.7 (d) c=0.7

Figure 5.3: Magnetization for a quadratically driven constraint term $\hat{H}_C$ for $c = 1$ in (a) and (b) and for $c = 0.7$ in (c) and (d). In the figures (a) and (c) we see the landscape for the magnetization for all values of s and λ. In (b) and (d) the actual magnetization for the way of QA and RA ($s = \lambda$) is shown.

annealing process which leads to the final ground state. QA will always start with a magnetization of 0, a superposition of all states, independent of the problem. We further keep in mind that these results are based on mean-field theory, does not include dynamics, $N \to \infty$ and $\beta \to \infty$, nevertheless it can give an approximation. In the next section 5.2 we will perform several simulations and measure the fidelity outcome. There the idea will arise to drive the constraint term $\hat{H}_C$ quadratically. Further information can be found in section 5.2, but here we want to investigate the resulting change in magnetization. This is shown in figure 5.3.

Comparing figure 5.1d with figure 5.3a we see a smoother transition from magnetization 0 (blue) to 1 (yellow). This is confirmed in figure 5.3b. We also see a changed behaviour in figure 5.3c (compared to 5.2c). The change in magnetization happens for higher s (and λ) values for QA (and RA). The jump remains but is here (in 5.3d) smaller for QA than in the previous one in 5.2c.

We conclude that the quadratic driven constraint term $\hat{H}_C$ does not change RA but can enhance QA for $c = 1$. The delay of the jump for RA with $c = 0.7$ can be useful in that sense, that the jump appears now when the transverse field is at its maximum (see the schedule in figure 4.1b). This means that in this region the fluctuations are at its maximum as well. This is an advantage over the linear

driven case when the jump appears with lower s values as the state has a smaller configurations space to explore and tunneling to far away local minima is less likely.
That a quadratic (or higher-order) driven constraint term $\hat{H}_C$ can enhance the performance of QA has also been shown in [39].
In the next section we will investigate if the results in this section can be confirmed.

5.2 Fidelity

In this section we perform simulation with the parameters mentioned in section 4.3. First we will discuss the results for the cases 1-4.

5.2.1 Case 1 and 2

The results for the ground state fidelity as a function of the computation time τ for $J = 1$ (case 1) and $J = -1$ (case 2) can be seen in figure 5.4. In 5.4(a) and 5.4(c) the constraint condition has been applied via 4-qubit-plaquettes. That means that auxiliary qubits are needed in the bottom lines which are fixed with $J_{aux} = 10$ to 1 (See chapter 2.4 and figure 2.3). With this modification a plaquette can be treated as the other but with the drawback of additional qubits. In the case of $N_l = 4$ this leads to 2 additional physical qubits, so $N_p = 6 + 2 = 8$ physical qubits. Without these auxiliary qubits one needs to modify the constraint condition in the bottom line. To satisfy the new condition 1 or all 3 qubits of a 3-qubits-plaquettes have to be 1. The results for this model are plotted in 5.4(b) and 5.4(d).
In the RA procedure we start with the ground state of $\hat{H}_1$. As we know from chapter 4.3.1, this is also the ground state of the final Hamiltonian for $J = 1$! This leads to good results for the ground state fidelity in figure 5.4 (a) and 5.4 (b).
The starting state for $J = -1$ can be seen in figure 4.3a as well as the final ground state in 4.3b. To reach the final ground state from the initial state 2 qubits need to get flipped during the anneal. The final state is 3-fold degenerated (see chapter 4.3.2). The results can be seen in figure 5.4 (c) and 5.4 (d).
The fidelity for $J = 1$ and $J = -1$ are significantly different for RA while the results for QA are similar. Furthermore, we can see a change of the fidelity for QA depending on which constraint condition has been used ((a) vs (b) and (c) vs (d)). The results for RA show no such dependence!
The reason for this could be the high local field $J_{aux} = 10$ and the 2 additional qubits as we already have a small system. With bigger system sizes this effect will probably vanish. Future work could investigate this behaviour in more detail.

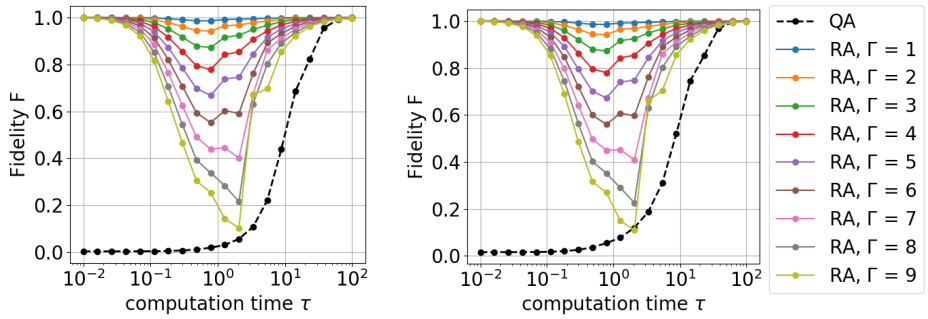

(a) Case1, $J = 1$, with auxiliary qubits

(b) Case 1, $J = 1$, without auxiliary qubits.

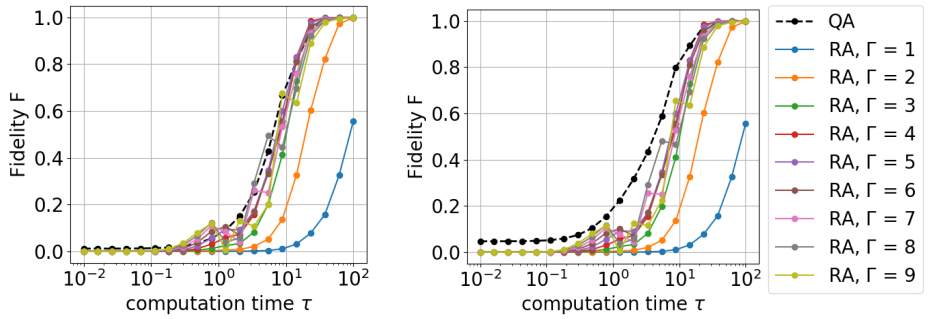

(c) Case 2, $J = -1$, with auxiliary qubits

(d) Case 2, $J = -1$, without auxiliary qubits.

Figure 5.4: Final ground state fidelities F for case1, $J = 1$, (figure (a) and (b)) and case 2, $J = -1$, (figure (c) and (d)) as a function of the total computation time for different values of Γ. The legend is valid for all subfigures. In figure (a) and (c) we have $N_p = 6$ physical qubits plus 2 auxiliary qubits in the bottom. With plaquettes consisting of 3 qubits in the bottom line of the LHZ-model the auxiliary qubits can be avoided. The results are plotted in figure (b) and (d).

5.2.2 Case 3 and 4

The other cases, case 3 and 4, of chapter 4.3 differ from the above mentioned cases by one element in the J_{ij} matrix. With $N_p = 6$ there are 6 elements in the interaction matrix, hence there are 6 different possible positions to set the inverted J ($J_{12}, J_{23}, J_{34}, J_{13}, J_{24}$ or J_{14}).
First we examine the results for setting all J to 1 except one to -1 (case 3), seen in figure 5.5. As we can see from these plots, it does not matter if we set J_{12}, J_{34} or J_{14} (figures 5.5a, 5.5c and 5.5f) to -1, we get the same results! The same holds for setting J_{13} and J_{24} (figures 5.5d and 5.5e) to -1. There is no other matching results for $J_{23} = -1$ (figure 5.5b).
The triplet J_{12}, J_{34} and J_{14} shows the best improvement over QA within all 6 cases. For $\Gamma = 5$ or $\Gamma = 6$ they return the maximum results for the fidelity, higher and lower Γ will return lower fidelity (figures 5.5a, 5.5c and 5.5f).
For the duo J_{13} and J_{24} we need to go up to $\Gamma = 7, 8$ to get the best results (figures 5.5d and 5.5e) and even then the fidelity is lower than in the previous case.
The unique case of J_{23} shows the worst results for RA of the different cases but

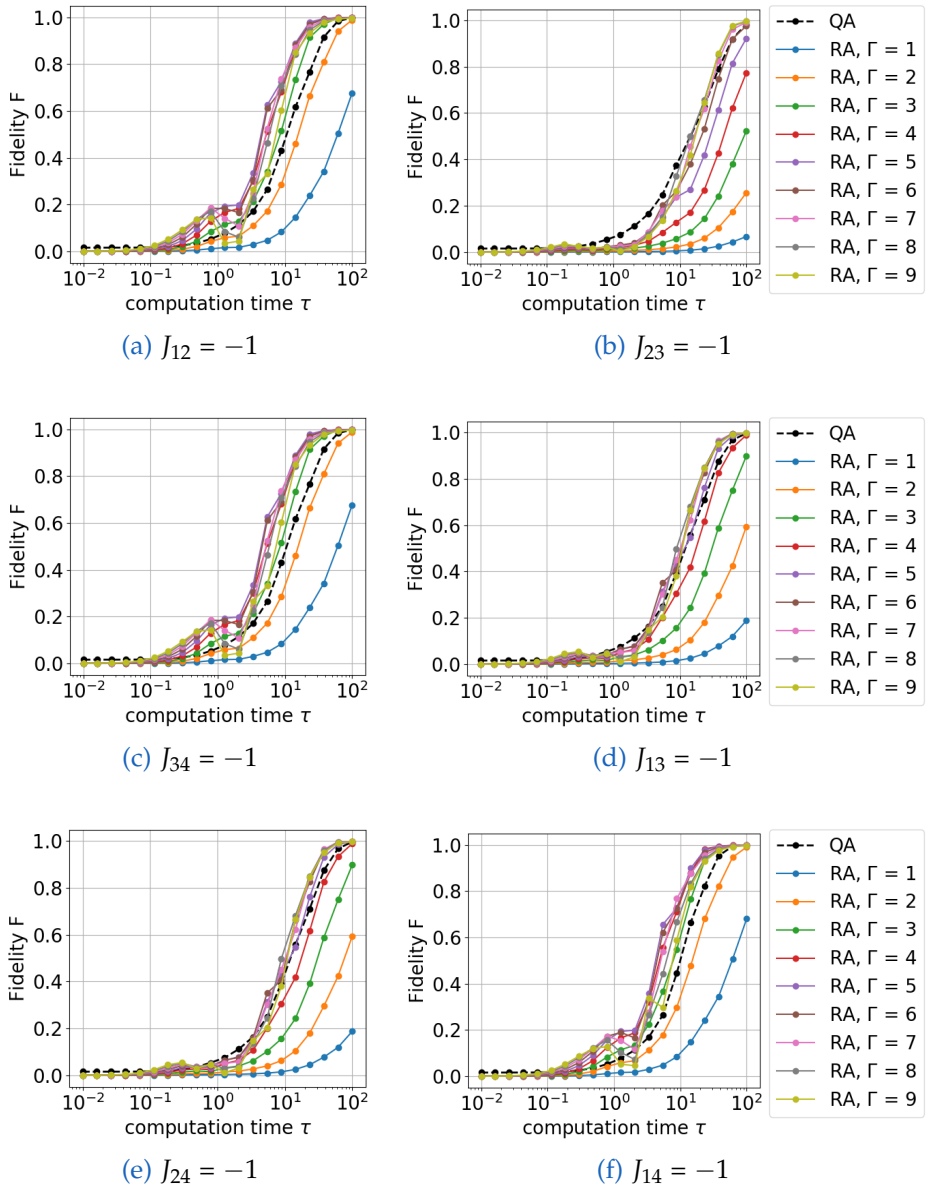

(a) $J_{12} = -1$ (b) $J_{23} = -1$

(c) $J_{34} = -1$ (d) $J_{13} = -1$

(e) $J_{24} = -1$ (f) $J_{14} = -1$

Figure 5.5: Final ground state fidelities F for case 3. All elements of the matrix J_{ij} are set to 1 except one is -1. There are 6 possible J_{ij} to switch for $N_p = 6$. The subplots are labeled with the inverted element J_{ij}.

for long computation times $\tau > 30$ it is still better than QA for $\Gamma > 7$.
If we invert the interaction matrix (all J to -1, except one J to 1, case 4) we receive the same results per J_{ij} as in figure 5.5 with two exceptions. The fidelity for putting J_{14} to 1 does not match with figure 5.5f (J_{14}=-1) but with figure 5.5b ($J_{23} = -1$) and $J_{23} = 1$ returns the same results as in figure 5.5f ($J_{14} = -1$).
With these 2 cases we ran 12 different simulation and get a total outcome of 3 different results. In table 5.1 this is summarized. 'Result 1' are the runs with the highest fidelity outcome and 'Result 3' with the one with the lowest. The J_{ij} marks which element of the interaction matrix is inverted. The results match for both cases only J_{14} and J_{23} are interchanged. To understand this outcome we need to look at the starting state and how to reach the final state. In both cases

Results	Case 3	Case 4
1	J_{12}, J_{14}, J_{34}	J_{12}, J_{23}, J_{34}
2	J_{13}, J_{24}	J_{13}, J_{24}
3	J_{23}	J_{14}

Table 5.1: Overview of matching results of case 3 and 4

one qubit needs to flip during the annealing process. We will see that for the best run (Result 1) the qubits at the corners (12, 34 and 14) are flipping. For the second-best (Result 2) the qubits at the places 13 and 24 need to change. The lowest fidelity returns the flip of the qubit at place 23 (Result 3). A more detailed explanation of the start and final states can be found in chapter 4.3.3 and 4.3.4. In other words we can say that flipping qubits at the corners of the LHZ, here qubit 12, 34 and 14, are the easiest for the annealing procedure. These qubits belong to 1 constraint plaquette. Then the qubits 13 and 24 follow, they are part of 2 constraint plaquettes. The hardest to flip is qubit 23 as it contributes to all 3 constraint plaquettes for $N_p = 6$.
The energy spectra of the RA process ($\tau = 10$, $\Gamma = 3$) of the just discussed cases can be seen in figure 5.6. $\Delta E = E_{ground} - E_i$ is the difference between the ground state energy $E_{ground} = E_0$ and the different eigenenergies $i \geq 0$ of the system at each time step. The thickness of the line is related to the fidelities $|\langle \Phi_i | \psi \rangle|^2$ of the evolving state $|\psi\rangle$ regarding the eigenstates $|\Phi_i\rangle$.
We can see from figure 5.6 that the energy gap between ground and first excited state gets smaller the more constraint-planquettes (left to right) are involved in flipping a qubit. Figure 5.6a (flipping of 1-constraint-qubit) shows the best result (F = 0.57, see title of each figures) and figure 5.6c (flipping of 3-constraint-qubit) shows the worst result (F = 0.06) for the ground-state fidelity. Following the thickness of the line, we can see that the evolving state 'leaves' the instantaneous ground state via the early smallest energy gap. QA starts in a superposition of states but in figure 5.7 we see that the dependence on the constraint qubit flip is

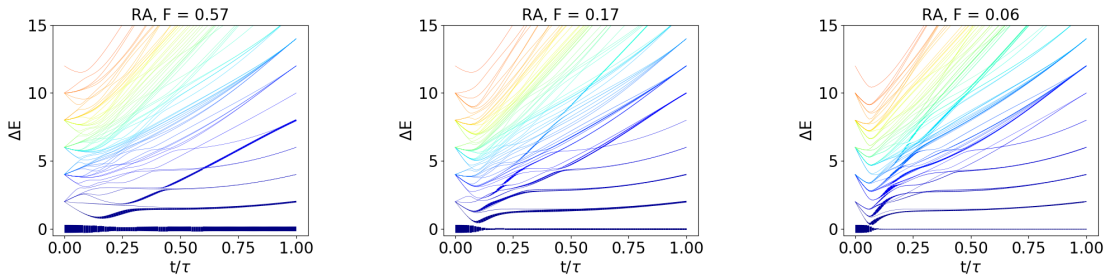

(a) RA, 1-constraint-qubit flip (b) RA, 2-constraint-qubit flip (c) RA, 3-constraint-qubit flip

Figure 5.6: Energy spectra of RA of flipping one qubit in the whole annealing process for $N_p = 6$, $\Gamma = 3$ and a total computation time τ of 10. The thickness of the lines is related to the fidelity of the evolving state to the eigenstates of the different eigenenergies at time t/τ. The fidelity relating to the actual final ground state in the end of the sweep can be read out in the title of each figure. $\Delta E = E_{ground} - E_i$ with $i \geq 0$

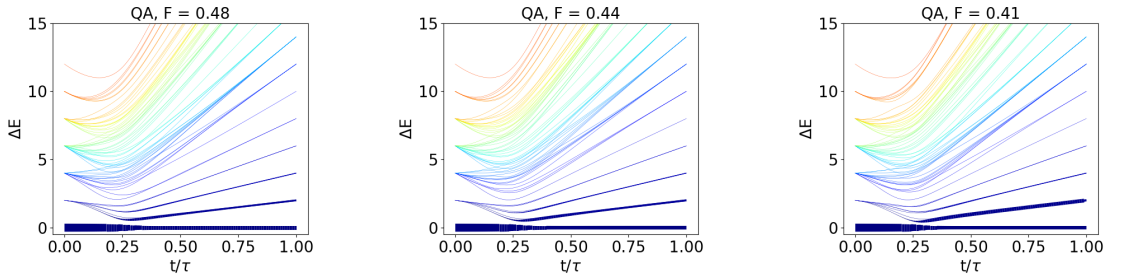

(a) QA analogon to RA 1-constraint-spin-flip

(b) QA analogon to RA 2-constraint-spin-flip

(c) QA analogon to RA 3-constraint-spin-flip

Figure 5.7: Energy spectra of QA for the same problems as in figure 5.6. Computation time τ is 10. The thickness of the lines is related to the fidelity of the evolving state $|\psi\rangle$ to the eigenstates $|\Phi_i\rangle$ of the different eigenenergies E_i at time t/τ. The fidelity relating to the actual final ground state in the end of the sweep can be read out in the title of each figure. $\Delta E = E_{ground} - E_i$ with $i \geq 0$

also present there. The QA analogon for a RA 1-constraint flip returns a better fidelity than the 2-, and 3-constraint flip but the effect is not as strong as in RA. We can note from this chapter that the constraints have a major influence in RA.

5.2.3 Random J_k

In this section the elements of the matrix J_{ij} can take random numbers between -1 and 1. The average of 120 runs can be seen in figure 5.8.
18 runs are trivial, the starting state is already the final ground state. These cases get separated from the non-trivial ones and can be seen in the right plot. For short $\tau < 0.005$ these runs return a fidelity of 1. The time is not long enough for the evolving state to explore the state space around it. It stays in the starting state which is the ground state. For higher τ and $\Gamma > 1$ the increased fluctuations allow the state to go around the phase space through quantum tunneling. The time τ however is not long enough. The evolving state gets trapped in a local minimum and returns a fidelity lower than 1. For computation times τ around

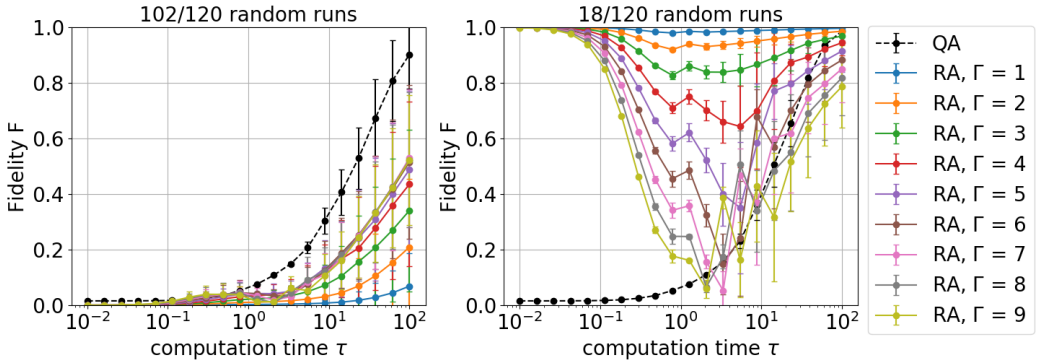

Figure 5.8: Average fidelity F over 120 random runs (102 non-trivial and 18 trivial). The interactions J are random values between -1 and 1.

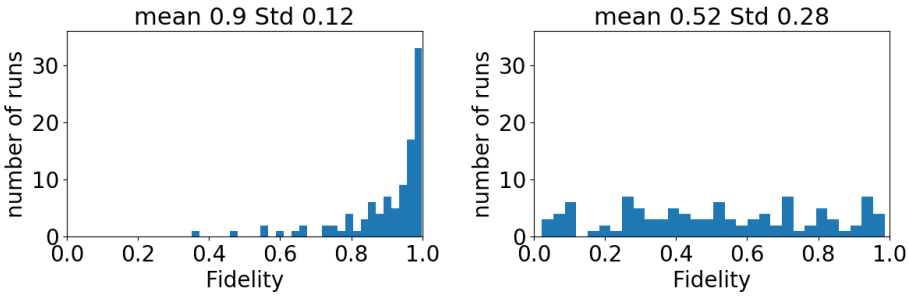

(a) QA (b) RA, Γ = 6

Figure 5.9: Histograms for 102 non-trivial runs of QA in (a) and RA for Γ = 6 in (b), τ = 100. The mean and the standard deviation Std are stated in the title of each figure.

1 the fidelity reaches its minimum. This effect is stronger for higher Γ. Longer times increase the fidelity again, the evolving state has time to optimize, but it wont go back to a fidelity of around 1 for $\Gamma > 3$.
Looking at the left plot we see that the non-trivial case for RA is significantly worse in terms of fidelity than QA. Especially RA with Γ = 1 does not come over 0.1 while QA reaches 0.9 at computation time τ = 100. RA improves for higher Γ but it starts to stagnate at Γ = 6. The exponential increase of fidelity over computation time τ is the expected behaviour as seen in other papers eg. [36].
We also note that the error bars are big, so we need to look at the actual distribution of the runs. Figure 5.9a shows us the histogram for QA at time τ = 100 (last point in the fidelity plot 5.8). The mean and the error (standard deviation Std) can be read out at the title. While the majority of the runs return a fidelity of over 0.8 there are a few exceptions. The histogram for RA in figure 5.9b show a different behaviour. The runs for Γ = 6 are evenly distributed over all fidelity values. This leads to a mean fidelity of 0.52 but a high standard deviation std of 0.28. One cannot give a correct estimation for RA, the outcome for Γ = 6 is random.

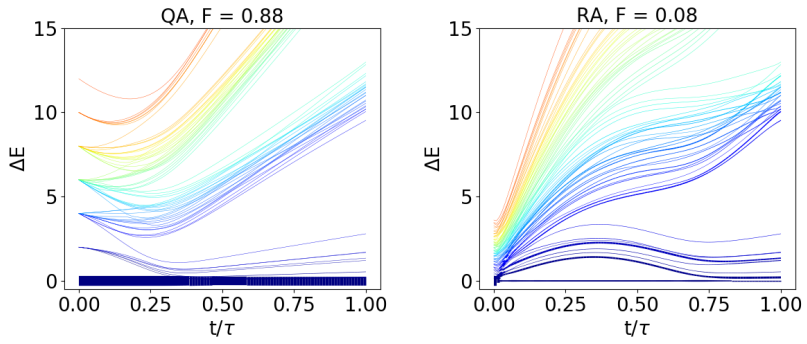

(a) QA (b) RA, Γ = 6

Figure 5.10: Energy spectra of random run #2 for QA and RA with Γ = 6. Computation time τ = 100. The thickness of the line is the overlap of the evolving state to the eigenstates of the different eigenenergies at times t/τ. Due to this thickness we can see when the evolving states 'leaves' the ground state. While QA shows a good behaviour, the evolving state for RA escapes immediately in the start to higher eigenstates. The fidelity F can be read out at the title of each figure.

This is a bad result and we need to clarify the cause. We look again at the energy spectrum. Random run #2 returns a low fidelity and the energy spectrum of QA and RA for $\tau = 100$ are plotted in figure 5.10. We label the individual runs from the 120 runs by #1 to #120 to be able to distinguish them. Random run #1 is a trivial run and has been neglected. The number has no further meaning.
Back to the plot, the thickness of the line represents again the fidelity $|\langle\Phi_i|\psi\rangle|^2$ of the evolving state $|\psi\rangle$ with the eigenstates Φ_i. QA can keep (most of) the evolving state in the ground state and ends with a fidelity of 0.88. RA returns a fidelity of 0.08 as the evolving state leaves the groundstate abrupt at the start of the anneal. This is due to the close eigenenergies at $t = 0$ and there is no way to avoid this with a smart choice of the annealing schedule. This problem never arises in QA as it starts in a superposition of all states and is always the same for fixed N_p.
The close eigenenergies arise from small values in the J matrix. To avoid this we need to modify the starting Hamiltonian $\hat{H}_{init} = \hat{H}_1$ to improve RA. This can be done in various ways. First let us divide the J matrix by the smallest element $|J_{min}|$ and let $|J_{min}|$ always be bigger than a certain threshold (here 0.017) to avoid computational problems. Note that just the J matrix in the initial Hamiltonian get modified. The J matrix in $\hat{H}_{LHZ}$ stay as it is.

Modification of the initial Hamiltonian

Running the same random runs, but with the modification of the initial Hamiltonian $\hat{H}_1^{mod}$ as mention above, we receive the results plotted in figure 5.11. Focusing on the left figure (the non-trivial runs) there is a significant improvement over the previous runs (figure 5.8). RA for $\Gamma = 3$ comes now over 0.8 for $\tau = 100$, whereas without the modification it was lower than 0.4. Higher Γ reach a fidelity higher than QA. We see the same behaviour as before: The improvement stagnates for stronger transverse fields $\Gamma > 5$. The best fidelities are reached by $\Gamma = 6$ and $\Gamma = 7$. The fidelity decreases for higher Γ.
The fidelity for the trivial runs in the right plot changed too. Higher Γ return a lower minimum for computation times τ around 1 than in the previous case. In addition all runs with different $\Gamma's$ are able to return to a fidelity of 1 for computation times $\tau > 30$.

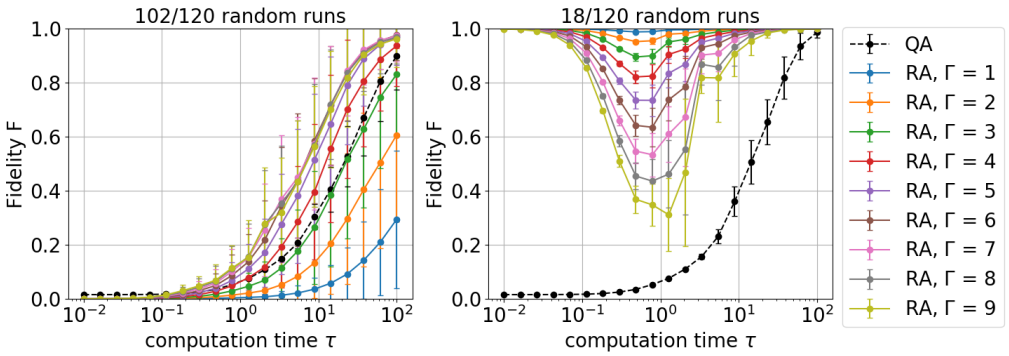

Figure 5.11: Average fidelity F over 120 random runs (102 non-trivial and 18 trivial) with modified initial Hamiltonian $\hat{H}_1^{mod}$.

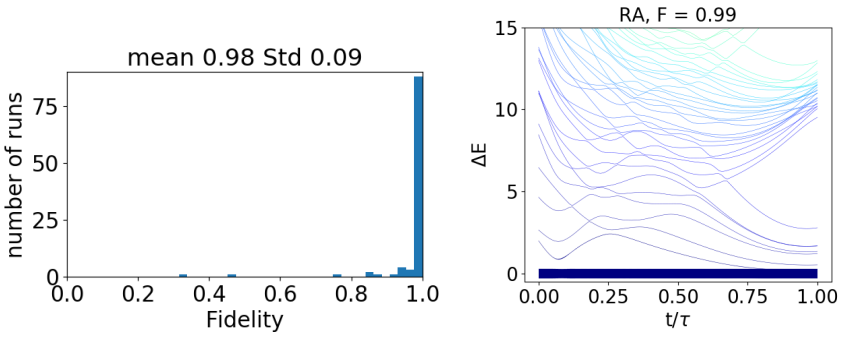

(a) Histogram, $\Gamma = 6$, modified $\hat{H}_{inital}$ (b) Energy spectrum, $\Gamma = 6$

Figure 5.12: The histogram in (a) shows the distribution of the runs for the modified RA with $\Gamma = 6$. Mean and standard deviation Std are stated in the title. The energy spectrum for run #2 is shown in (b). Computation time $\tau = 100$ for both plots.

As in the previous runs we will investigate the results with histograms. The histogram for RA with the modified initial Hamiltonian in figure 5.12a shows a significant improvement over the original RA in figure 5.9b but is also more peaked at a fidelity of 1 than the distribution for QA in figure 5.9a.
Furthermore, we can compare the energy spectrum in figure 5.12b with the spectrum in figure 5.10b. Due to the modification of the initial Hamiltonian the energy bands are more spread out in the start. The evolving state can not 'escape' the instantaneous ground state in the beginning of the anneal. It returns a fidelity of 0.99 instead of 0.08.

Quadratic drive of the constraint term

In section 5.2.1 we figured out that the performance of RA strongly depends on which qubits flip during the annealing process. This is due to the constraints. In figure 5.6 the flip of a 3-constraint qubit returns the earliest and sharpest energy gap.
This knowledge leads us to the thought of what will happen if we turn on the constraint Hamiltonian $\hat{H}_C$ slower. To achieve this, we modify the RA-Hamiltonian of equation 4.1 to

$$\hat{H}_{RA} = (1 - s_t)(1 - \lambda_t)\hat{H}_1^{mod} + s_t\hat{H}_1 + s_t^2\hat{H}_C + (1 - s_t)\lambda_t\Gamma\hat{V}_{TF} \tag{5.4}$$

Instead of driving $\hat{H}_C$ linearly we turn it on quadratically. We also keep the modified initial Hamiltonian denoted as $\hat{H}_1^{mod}$ from the previous section. Running the simulations from section 5.2.1 again we obtain new energy spectra for the 1-, 2- and 3-constraint qubit flip. We can see them in figure 5.13 and can compare it to figure 5.6. We see the same connection for 1-, 2- and 3-constraint qubit flip to the minimal energy gap but it happens later than in the previous runs. We also notice that the fidelity improves significantly. The resulting fidelities are summarized in table 5.2.

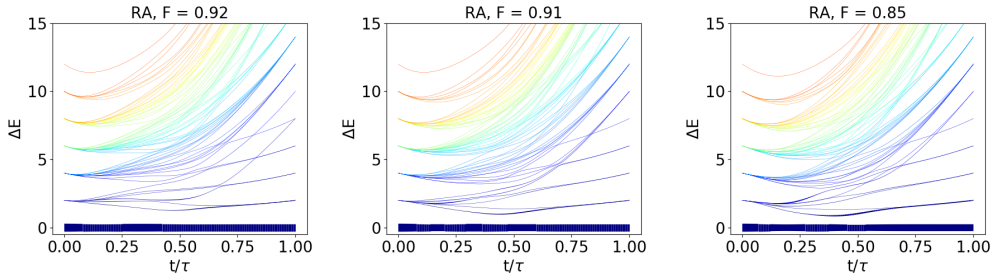

(a) RA, 1-constraint-qubit flip (b) RA, 2-constraint-qubit flip (c) RA, 3-constraint-qubit flip

Figure 5.13: Energy spectra of RA with a quadratic driven $\hat{H}_C$ for case 3 and 4 (flipping one qubit in the whole annealing process) for $N_p = 6$, $\Gamma = 3$ and a total computation time τ of 10. The spectra for a linear driven $\hat{H}_C$ are plotted in figure 5.6. The fidelity relating to the final ground state can be read out in the title of each plot.

	F_{linear}	$F_{quadratic}$
1-constraint qubit flip	0.57	0.92
2-constraint qubit flip	0.17	0.91
3-constraint qubit flip	0.06	0.85

Table 5.2: Fidelities F for case 3 and 4 for linear and quadratic driven constraint Hamiltonian $\hat{H}_C$

The fidelity $F_{quadratic}$ for a 3-constraint qubit flip is 14 times bigger than F_{linear} just by turning on the constraint Hamiltonian $\hat{H}_C$ slower. The effect is not as strong in the 1- and 2-constraint qubit flip but still significant.
In that sense, we run the 120-random J simulations for the new RA Hamiltonian 5.4 again. The results for the fidelity are shown in figure 5.14.
Compared to the previous results in figure 5.11 we notice that the slower start of the constraint term $\hat{H}_C$ impacts low $\Gamma's$ the most. For the non-trivial runs (left plot) the blue line for $\Gamma = 1$ now reaches almost 0.6 at $\tau = 100$, before it was at about 0.3. Also the green line for $\Gamma = 3$ improves and is now higher than the black line for QA. $\Gamma = 5$ and $\Gamma = 6$ return the best results for the fidelity. Higher Γ decrease the performance of RA again. The maximum reached in the linear and quadratic schedule are similar.
The trivial runs (right plot) return lower minima for the fidelity but are otherwise similar to the linear driven case.
In figure 5.15 we see the direct comparison of the maximal fidelities reached in the quadratic and linear schedule. Both cases can compete with each other at $\tau > 40$, but the quadratic outperforms the linear one in the middle regime $2 < \tau < 40$.
For further investigation we will compare the histogram and the energy spectrum of run #2 in figure 5.16 with the linear driven case in figure 5.12. The 102 random runs for RA with $\Gamma = 6$ and $\tau = 100$ returns a similar plot for the quadratic and linear driven constraint term: $F_{linear} = 0.98 \pm 0.09$ and $F_{quadratic} = 0.97 \pm 0.10$. While the fidelity is by 0.01 lower the spectrum for run #2 (figure 5.16b returns a slightly better fidelity for the quadratic case. The minimum energy gap in the beginning of the anneal is much more present in the linear driven spectrum

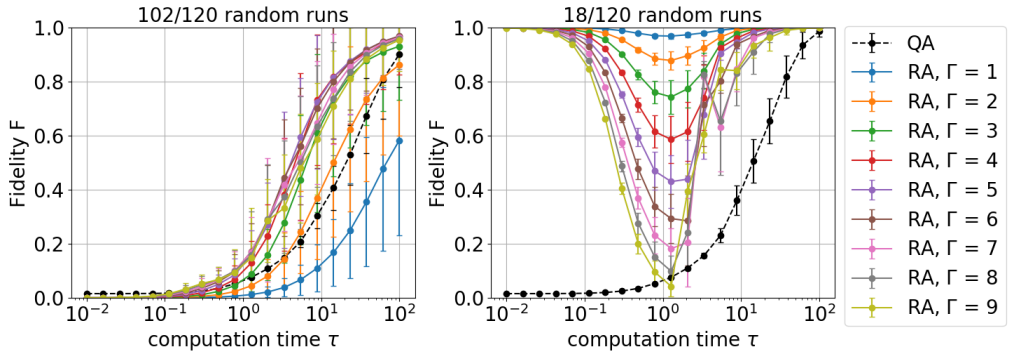

Figure 5.14: Average fidelity F over 120 random runs (102 non-trivial and 18 trivial) with modified initial Hamiltonian and a quadratic driven constant term $\hat{H}_C$.

(figure 5.12b).

To see how a quadratic driven $\hat{H}_C$ affects the individual runs we will look at the difference in fidelites. $F_{quadratic} - F_{linear}$ for each run are plotted in figure 5.17. A positive value means that the quadratic run provides the better fidelity. This is done for low, middle and high Γ-values for 2 different computation times, namely $\tau = 14$, shown in 5.17a, and $\tau = 100$, shown in 5.17b.

In both cases we see that for low Γ ($\Gamma = 1 - 3$) the quadratic drive of $\hat{H}_C$ results in a better fidelity (with a few exceptions). This effect is still present for $\Gamma = 4 - 6$ with $\tau = 14$ but the amount of cases where F_{linear} is higher than $F_{quadratic}$ increases. For $\Gamma = 7, 8, 9$ there are almost as many cases with a higher F_{linear} than with $F_{quadratic}$. This looks different for higher computation times, seen in figure 5.17b. While $\Gamma = 1, 2, 3$ shows a clear improvement of the fidelity for the quadratic schedule the results for $\Gamma = 4, 5, 6$ and $\Gamma = 7, 8, 9$ show less dependence on $\hat{H}_C$. For $\Gamma = 7, 8, 9$ we see more runs with a higher F_{linear}.

Summarizing the results, we see an improvement of the fidelity for a quadratic driven constraint term $\hat{H}_C$ for $\Gamma = 1, 2, 3$ for all computation times τ. For $\Gamma = 4, 5, 6$ and times $2 < \tau < 40$ it can outperform the linear driven schedule as well. However, the maximum reached does not differ compared to the linear driven schedule for $\tau > 40$. This is related to the result in figure 5.17b. Long computation times like $\tau = 100$ for $\Gamma = 4, ..., 9$ show almost no dependence on the annealing schedule used.

Furthermore we can compare these results now with the outcome of the previous

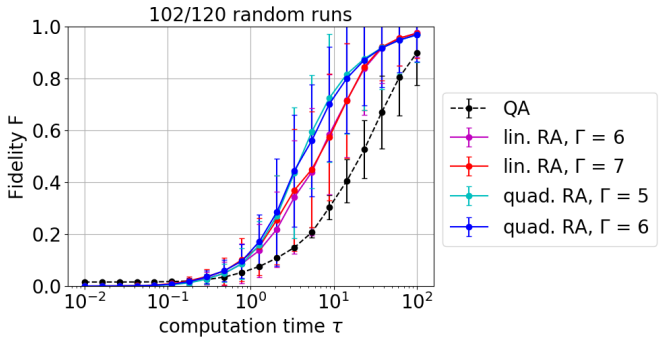

Figure 5.15: Direct comparison of the maximal fidelities reached for RA with linear and quadratic driven constraint term $\hat{H}_C$.

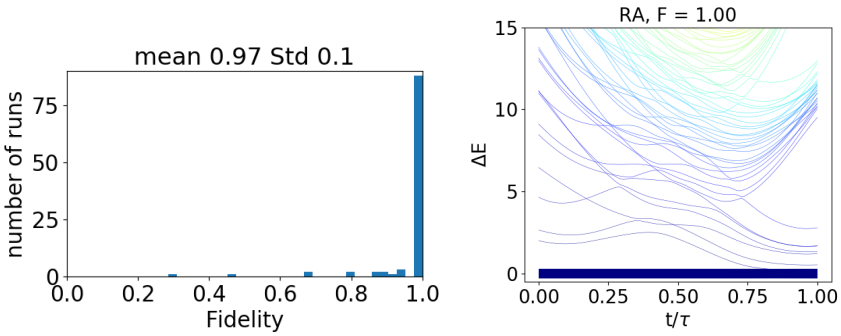

(a) Histogram, $\Gamma = 6$, modified $\hat{H}_{inital}$ and quadratic driven $\hat{H}_C$

(b) Energy spectrum, $\Gamma = 6$

Figure 5.16: The histogram in (a) shows the distribution of the runs for the modified RA with $\Gamma = 6$. The energy spectrum for run #2 is shown in (b). Computation time $\tau = 100$ for both plots.

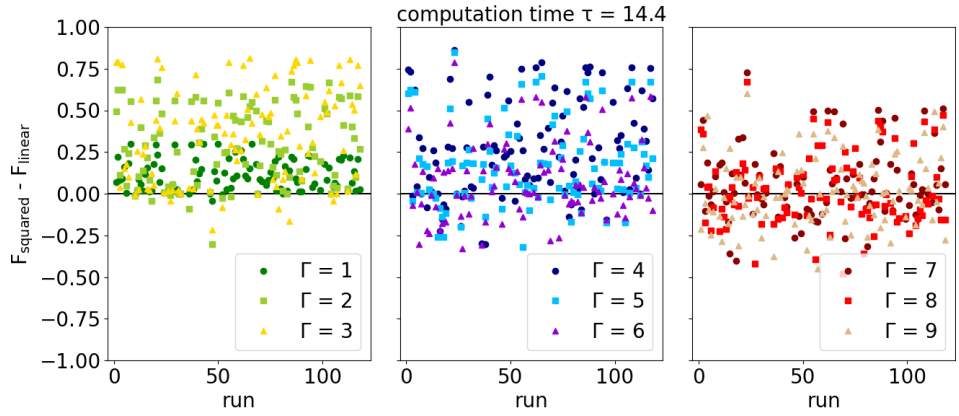

(a) $\tau = 14$

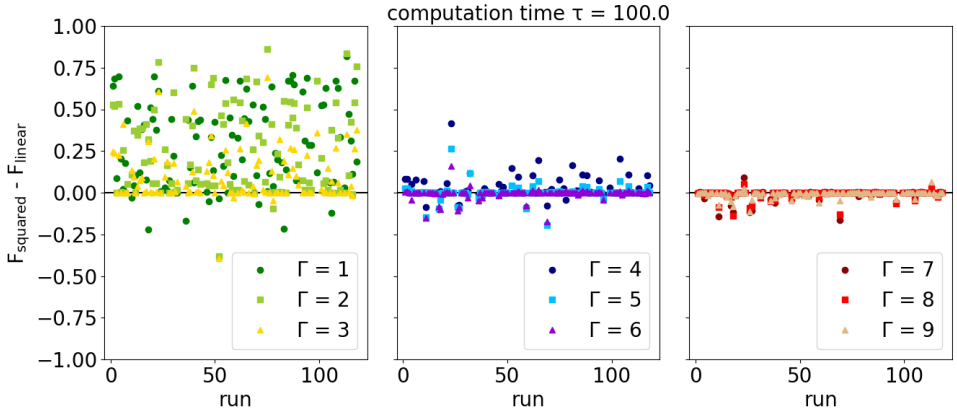

(b) $\tau = 100$

Figure 5.17: Comparison of the fidelities of RA with linearly driven (F_{linear}) and quadratically driven ($F_{quadratic}$) constraint term for all non-trivial runs. On the y-axis the difference between $F_{quadratic}$ and F_{linear} are plotted. A positive value means that $F_{quadratic}$ is higher than F_{linear}. The x-axis is labeled with the individual runs #1 to #120 except for the trivial ones. This is shown for computation time $\tau = 14$ (b) and $\tau = 100$ (b).

section 5.1. The analytic for the magnetization showed as an advantage for a quadratic driven constraint term $\hat{H}_C$. This matches with the outcome of this results. Nevertheless, the formula for the magnetization 3.34 with $N \to \infty$ does not distinguish between the places of the qubits. Also the results for case 2 $c = 0$ ($J = -1$) wont match. The analytics showed the same results for case 1 and 2 but the actual fidelities differ significantly. The reason lies in the finite amount of qubits. With $N_p = 6$ we do net get a final ground state with a magnetization of -1 for case 2 as the solution consists of 4 1-valued qubits and 2 0-valued qubits. The 0-valued qubits are due to the constraints and have less influence the bigger the system size N.
How the results of this chapter are related to the minimal energy gap $\Delta E_{1,0}$ will be investigated in the next section.

5.3 Minimal energy gap

Looking at the energy spectrum in figure 5.13 we noticed that the minimal energy gap $\Delta E_{1,0}$ appears later and not as small as in the linear case in figure 5.6. To see if this is true for the random runs we average $\Delta E_{1,0}$ over all 120 runs. The result is shown in figure 5.18. The results are valid for all computation times τ. Again the non-trivial (right) and trivial (left) runs are separated. The error bars are plotted in horizontal direction for a better overview. For rising Γ in the non-trivial runs the gap $\Delta E_{1,0}$ but also the standard deviation increases. While QA non-trivial (trivial) returns $\Delta E_{1,0} = 0.26 \pm 0.14$ (0.47 ± 0.12), RA $\Gamma = 9$ gives for $\hat{H}_C$ quadratic $\Delta E_{1,0} = 0.73 \pm 0.49$ (1.51 ± 0.46). This is a high standard deviation for RA and shows how different the energy spectrum for different problems can be.

Focusing on the non-trivial runs we see great improvement of the gap $\Delta E_{1,0}$ for $\hat{H}_C$ quadratic $\Gamma = 1, 2, 3$ over $\hat{H}_C$ linear. This is in agreement with the good improvement of $\Gamma = 1, 2, 3$ seen in 5.17. However, the minimal gap $\Delta E_{1,0}$ stops getting bigger with the transverse field for $\Gamma > 4$ for quadratic and for $\Gamma = 6$ for linear $\hat{H}_C$. In fact $\Gamma = 7$ (9) shows the biggest minimal energy gap $\Delta E_{1,0}$ for the quadratic (linear) schedule. This does not relate to the best fidelity outcome in figures 5.14/5.11.
We also see interesting behaviour in the trivial runs. The gap for RA is double the size of the maximum in the non-trivial runs. There is no Γ dependence and no significant difference to $\hat{H}_C$ quadratic and linear. Also the gap for QA is bigger

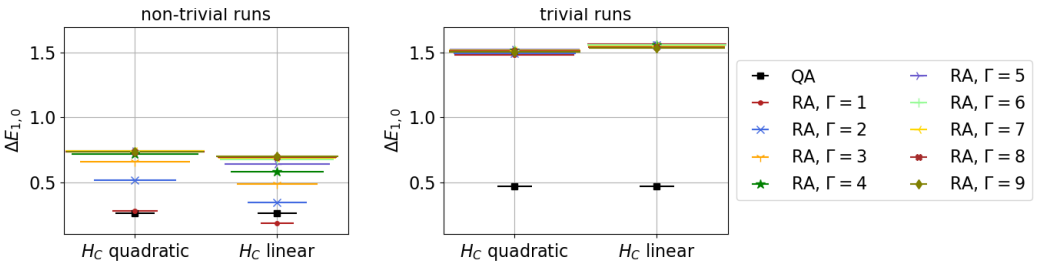

Figure 5.18: Comparison of the minimum energy gap for the linear and quadratic RA schedule. In the left plot we see the non-trivial and in the left the trivial runs.

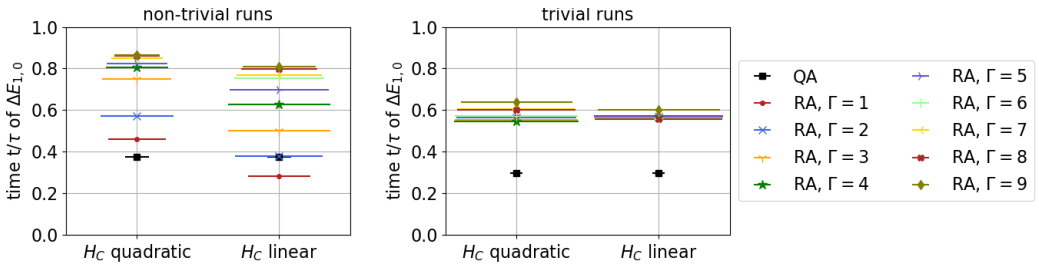

Figure 5.19: Comparison of the time t/τ when the minimum energy gap arises. In the left plot we see the non-trivial and in the left the trivial runs.

than the non-trivial one. According to this result the trivial runs for RA are also easier to solve for QA.
To understand this we remind ourselves that the trivial runs for RA where those where the starting state does not violate any constraints. QA can anneal from a superposition into the solution state without dealing with complicated constraints optimizations.
The size of the energy gap $\Delta E_{1,0}$ gives a good indication for the 'difficulty' of the problem but also when it arises is important. If the gap arises early in our energy spectrum the state has no time to change as the strength of the transverse field is too low (and therefore the fluctuations are too weak).
The average of the time of $\Delta E_{1,0}$ is shown in figure 5.19. Again the standard deviation for RA is big. While the gap for QA arises at $t/\tau = (0.37 \pm 0.08)$ (0.30 ± 0.04) non-trivial (trivial), for RA $\Gamma = 2$ it happens at $t/\tau = (0.57 \pm 0.26)$ (0.56 ± 0.42) non-trivial (trivial) for $\hat{H}_C$ quadratic. This shows again how unpredictable the spectrum of an RA sweep is. For every problem it has different starting values. QA has always the same.
In general the gap arises later for non trivial runs with a quadratically driven $\hat{H}_C$. The increase of the transverse field 'delays' the gap nevertheless the behaviour is different than the one seen with the gap $\Delta E_{1,0}$. In all cases the latest gap $\Delta E_{1,0}$ arises with $\Gamma = 9$. This does not match with the best fidelity outcome.
To summarize the results we can say that a quadratic drive of the constraint Hamiltonian $\hat{H}_C$ delays and increases the energy gap $\Delta E_{1,0}$ especially for $\Gamma = 1, 2, 3$ compared to the linear drive. The gap and time are rising with higher Γ but the biggest and latest gap $\Delta E_{1,0}$ does not result in the best fidelity outcome.
Furthermore the gap $\Delta E_{1,0}$ does not depend on the computation time τ. The behaviour seen in figure 5.17b, that the performance of the anneal for $\tau = 100$ and $\Gamma > 4$ does not show the influence of the schedule used as shorter computation times τ, can not be explained by the size and time of the minimal energy gap $\Delta E_{1,0}$.

5.4 Variance of energy

In the histograms of the previous section we see the same exceptions with $F < 0.5$ for RA 5.12a, 5.16a and QA 5.9a. This means that there are runs which are hard to solve for both RA and QA.

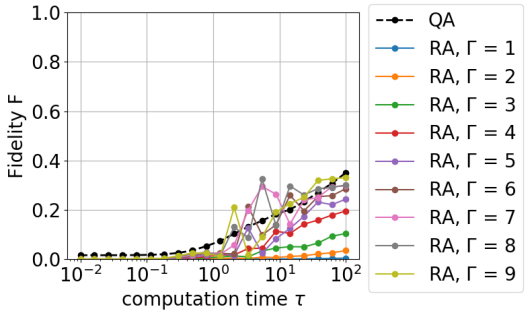

Figure 5.20: Fidelities F of run #32 over different computation times τ with a quadratic driven $\hat{H}_C$.

The fidelities for run #32 are shown in 5.20. Within this run we receive the lowest fidelity outcome in both RA and QA with $\tau = 100$, namely $F = 0.29$ for RA $\Gamma = 6$ and $F = 0.35$ for QA. In addition the simulations with RA $\Gamma > 4$ show a not known 'zig-zag' behaviour.

To be able to explain this behaviour we look again at the energy spectrum, it is shown in figure 5.21. We see the spectra for RA $\Gamma = 6$ with computation time $\tau = 1$, $\tau = 10$ and $\tau = 100$. In all cases it looks like we are dealing with a degenerate groundstate but this is not true. The groundstate and the first- and second-excited state energy are so close to each other that we can not distinguish it by eye.

E_0	E_1	E_2	E_3	E_4
-16.11	-16.09	-16.03	-15.59	-15.45

Table 5.3: Groundstate energy E_0 and the 4 lowest excited state energies for run #32

In table 5.3 we can find the lowest eigenenergies of run #32. The groundstate energy E_0 and the first (second) excited state energy E_1 (E_2) are separated by $\Delta E = 0.02$ (0.08). The difference to the third excited state energy E_3 is $\Delta E = 0.52$. We also need to note here that the spectrum of the figures in 5.21 would return a minimal energy gap $\Delta E_{1,0}$ at time $t/\tau > 0.75$ but this gap is due to the close eigenstates and can not be related to a phase transition.
In figure 5.21 we see due to the thickness of the line, when the evolving state leaves the ground state. For $\tau = 1$ this happens early and we see a respective amount in energies higher than E_8. This is not true for computation time $\tau = 10$. We 'lose' the evolving state for $t/\tau > 0.75$ to energy states of $E_1 - E_5$. For $\tau = 100$ the evolving state energy is a combination of E_0, E_1 and E_2 which are separated by $\Delta E = 0.08$. The ground state fidelity is $F = 0.29$ and the fidelities for the first and second excited states are $F_1 = 0.65$ and $F_2 = 0.06$. Adding the fidelities up returns a fidelity of $F_{0-2} = 1.00$ for $\tau = 100$.
The solution state may wont give the best result but the energy is still low and close to the best solution. The low ground state fidelity of $F = 0.29$ does not give us this information.
In figure 5.22 we can see the severity of this problem. We see the energy spectra of RA, $\Gamma = 9$, random run #28 for computation times $\tau = 1$ and $\tau = 10$. The fidelity

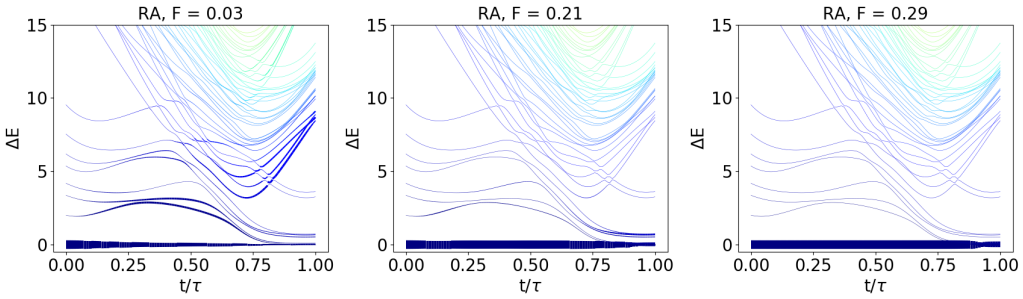

(a) $\tau = 1$ (b) $\tau = 10$ (c) $\tau = 100$

Figure 5.21: Energy spectra for RA $\Gamma = 6$ run #32 with computation times $\tau = 1$ in (a), $\tau = 10$ in (b) and $\tau = 100$ in (c).

for $\tau = 1$ is $F = 0.28$ and for $\tau = 10$ it is $F = 0.19$. While we gain a higher fidelity for the first case we see in the spectrum that the evolving state escapes to higher energy states. $\tau = 10$ returns a lower fidelity but the state in the end of the sweep is a combination of lower energy states. Therefore, the annealing run for $\tau = 10$ returns states, beside the groundstate, of lower energy than the one in $\tau = 1$ even tough it returns the higher fidelity. This also explains the 'zig-zag' behaviour seen in figure 5.20.

One way to deal with this problem (besides higher computation times τ) is to avoid the transitions to higher energies. This can be done by artificially spreading the eigenenergies in the end of the sweep in the same way as we did with the initial Hamiltonian $\hat{H}_1$. Another way is to change the schedule of the transverse field. The eigenenergies are close but that does not mean that the corresponding eigenstates are close in the configuration space. It could make sense to keep the transverse higher towards the end but maybe also decreasing it will lead to a better result. Future work needs to investigate this problem.

It also make sense to discuss at his point if the measurement of the fidelity is enough to give information of the success of the annealing run as it concerns both RA and QA. The fidelity gives us information how much of the solution state overlaps with the ground state but there is no information about the other parts of the state. There is no indication on how close the remaining part is to the lowest energy with $F < 1$.

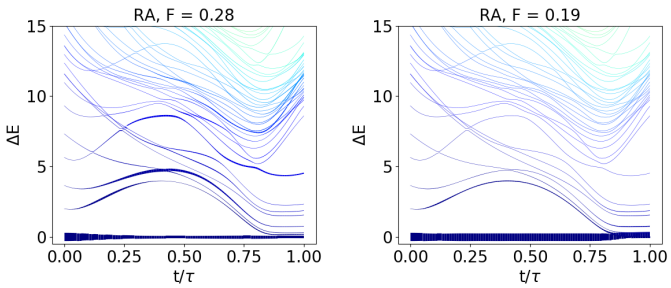

(a) $\tau = 1$ (b) $\tau = 10$

Figure 5.22: Energy spectra for RA $\Gamma = 9$ run #28 with computation times $\tau = 1$ in (a), $\tau = 10$ in (b).

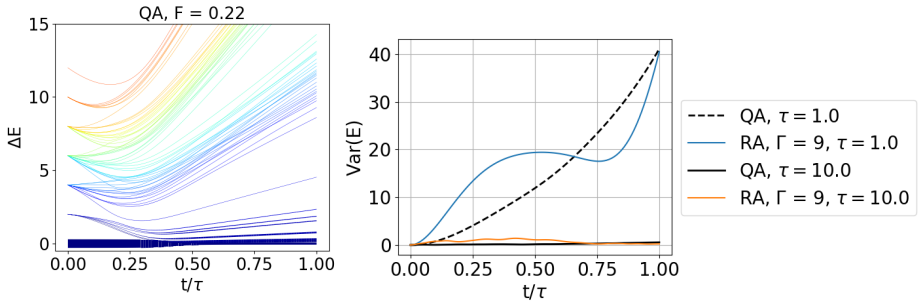

(a) Spectrum of QA, $\tau = 10$ (b) Variance of energy

Figure 5.23: The energy spectrum for #28 of QA $\tau = 10$ is shown in (a). In (b) the energy variance of run #28 for QA and RA $\Gamma = 9$ with $\tau = 1$ and $\tau = 10$ are plotted. The corresponding energy spectra for RA can be found in figure 5.22.

The variance can be an interesting measure for this. In figure 5.23b we see the variance of the energy for the QA and RA run #28 over the annealing time t/τ for $\tau = 1$ and $\tau = 10$. The simulations with a computation time of $\tau = 1$ raise to higher values than the one with $\tau = 10$ even though RA $\tau = 1$ returns a higher fidelity than RA $\tau = 10$. The corresponding energy spectra for the RA runs are shown in 5.22. The increase of the energy variance over time also shows us when the evolving state is leaving to higher energies. In figure 5.23a we see the spectrum of QA for run #28. The corresponding RA spectrum is shown in 5.22b. QA reaches a fidelity of $F = 0.22$ and RA $F = 0.19$. However the variance of the energy is 0.55 (0.23) in the end of the sweep for QA (RA). This means QA gains a better fidelity but also a higher energy variance. Adding up the fidelities for the 3 lowest eigenstates gives $F_{0-2} = 0.68$ for QA while it was $F_{0-2} = 1.00$ for RA. This matches with the outcome of the energy variance.
Nevertheless the variance should also be treated with caution. It characterizes the distribution around the mean value. If the evolving states escapes completely to higher energies it would provide us with the wrong information.
In figure 5.24 we see the mean values for the energy variance at $t/\tau = 1$ for the linear and quadratic driven process. The plots start from computation time $\tau = 5$ as this is the time where the mean fidelity is about $F = 0.5$. With this we can avoid the just mentioned problem.
Figure 5.24a shows the variance for the linear schedule. In the left plot we see the results for the non-trivial runs. The line for RA $\Gamma = 1$ can not bee seen as it returns a energy variance higher than 8. The variance decreases for higher Γ. $\Gamma = 4 - 9$ reach lower values than QA for higher computation times τ but for times $\tau < 10$ QA shows the best results. Within RA, $\Gamma = 9$ returns the best values. Nevertheless the fidelities in figure 5.11 are the best for $\Gamma = 6, 7$. The biggest energy gap in figure 5.18 is found for $\Gamma = 9$ which matches with the outcome of the energy variance.
The variance of the trivial runs show the same behaviour as the fidelities in 5.11. Looking at the quadratic case in figure 5.24b we see the best results in RA for $\Gamma = 7 - 9$. For some computation times τ $\Gamma = 7, 8$ are better than $\Gamma = 9$. The difference is small, but this behaviour can also be seen in the plot for the size of the energy gap, figure 5.18, where the highest gap occurs for $\Gamma = 7$. However, the

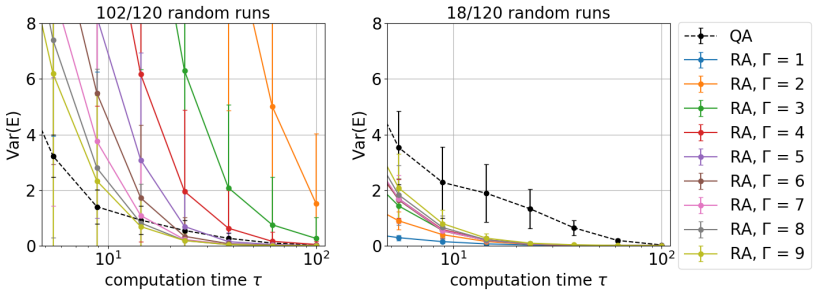

(a) linear $\hat{H}_C$

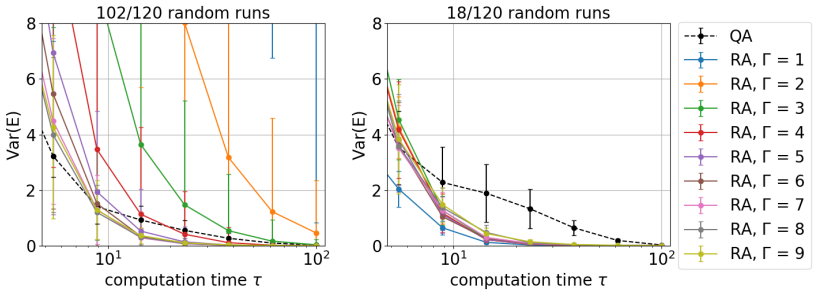

(b) quadratic $\hat{H}_C$

Figure 5.24: Mean energy variance Var(E) at $t/\tau = 1$ over computation time τ for the linear (a) and quadratic (b) driven schedule.

best fidelities are achieved for $\Gamma = 5, 6$ (figure 5.14). In general the variances for the non-trivial runs improved over the linear driven case in figure 5.24a. This is not true for the non-trivial runs, they are better in 5.24a.
To summarize the results in this section we can say that we need to treat the fidelity with caution. While the fidelity for RA $\Gamma = 6$ is higher than the one for $\Gamma = 9$ the resulting state has a higher energy for $\Gamma = 6$ than $\Gamma = 9$. This is due to the close lowest eigenenergies in the end of the sweep. The results for the energy variance, figure 5.24, agree with the outcome of the minimal energy gap $\Delta E_{1,0}$, figure 5.18.

6 Discussion and conclusion

In chapter 5 we showed the results of analytical and numerical investigations. In this chapter we want to summarize and discuss the outcome which will be followed by a conclusion.
Section 5.1 is showing the analytical results. They show that RA has an advantage over QA by avoiding and weakening a jump in magnetization. This is because the system already has information about the problem. Nevertheless, the results are based on several approximations, there will be other effects that influence the outcome. For example it won't be possible to achieve zero temperature in a quantum annealer. This concerns both RA and QA. However, here we want to focus on the differences in the numerical results in section 5.2. First of all the formula for the magnetization 3.34 does not distinguish between the individual qubits. In section 5.2 we found out that the results for the fidelity depend strongly on which qubit is flipped during the annealing process. Flips of qubits that are part of fewer constraint plaquettes return better results. This is the outcome for $N_p = 6$ qubits, but the analytical results are for $N_p \to \infty$. A qubit can be part of a maximum of 4 constraint plaquettes, even for $N_p \to \infty$. The number of 1-constraint qubits stays the same for different system sizes N: they are the 3 qubits in the corners of the LHZ. In addition to this, also the 2- and 3-constraint qubits can be neglected compared to the amount 4-constraint qubits for large system sizes N. This is in agreement with the analytical results.
Another difference due to finite size is the result for $J = -1$ (case 2, $c = 0$). In the analytical results, figure 5.2a the magnetization does not change throughout the annealing process. With $N_p = 6$ we start with a configuration of 0-values (spin down) qubits due to $J = -1$. This is a relative magnetization of $m = -1$. The solution configuration consists of 4 0-values (spin down) qubits and 2 1-values (spin up) qubits and therefore the magnetization is $m = -0.33$. This means that the magnetization will change over the annealing process. In the simulation we received better fidelities for QA with $J = -1$ (figure 5.4d) which is the opposite of what we expected based on the analytics. We can assume that RA will gain an advantage for bigger system sizes in this specific case. However, future work should investigate the behavior of the fidelity over the system size N as well as the magnetization for smaller systems.
In section 5.2.1 we detected differences in fidelity for QA with and without auxiliary qubits. There is no difference for RA. It may depend on the strength of the local field J_{aux} acting on these qubits. This effect may vanish for $N_p \to \infty$. It is possible to build an LHZ without these additional qubits but future work can investigate this behavior.
The best fidelity achieved in section 5.2.3, figure 5.14 for random fields J does not match with the biggest and latest minimal energy gap $\Delta E_{1,0}$ in section 5.3, figure

5.18, but the smallest energy variance in section 5.4, figure 5.24b, does! This is due to the fact, that the fidelity does not provide sufficient information about the success of the annealing run. This is more explained in section 5.4. The variance (not just the energy variance) can also give information about when the evolving state is leaving the instantaneous ground state providing that it does not escape completely to higher states. How this can be used in actual physical devices still needs to get discussed.
Furthermore we increased the performance of RA significantly with a modified initial Hamiltonian. There are also other ways to modify it, like setting all elements to 1 and use the signs of the actual J matrix. Another performance gain is possible by solving the problem of the close energy bands of the ground and the first excited state at the end of the annealing process. Changing the annealing schedule by different driving of the transverse field V_{TF} or modification of the J-matrix can be tools to achieve this. Nevertheless, the J-values are strongly related to the actual time used in the lab (see section 4.2).
With the modified initial Hamiltonian, RA achieves a better result, but we can make a further improvement with a quadratic driving of the constraint Hamiltonian $\hat{H}_C$, see figure 5.24b and 5.24a. In both cases high $\Gamma = 7, 8, 9$ achieve the best results and the difference between them can be seen in the middle regime $\tau < 40$. For smaller Γ the quadratic case achieves a significantly better performance than the linear one. However, it is not discussed yet if a high transverse field is problematic for the actual physical implementation of a quantum annealer.
It is also not proven that a quadratic drive of the constraint Hamiltonian $\hat{H}_C$ gives the best results. The original idea was to start the constraint term slower as it influences the performance, shown in figure 5.6. In the paper [39] it is shown that one can avoid first-order phase transitions already with a non-linear drive of $s^{1.56}\hat{H}_C$ for QA. In this work the RA Hamiltonian has been modified, not the QA Hamiltonian. Further work can be done to find the critical point and the best schedule for RA.
We used 2 parameters s and λ for our annealing process. It is possible to introduce a third one which could, with a smart choice, improve the performance.
Overall, we outperform QA with RA, a quadratic drive (equation 5.4) achieves better results than the linear drive 4.1. Due to the high and late energy gaps seen in figures 5.18 and 5.19 we can say that quantum phase transitions are not the major problems in RA in the LHZ-model. The main problems are the close eigenenergies in the beginning and the end of the annealing procedure. To avoid the closes energy bands in the beginning one can modify the initial Hamiltonian as states in this thesis or by using a new Hamiltonian with 1 and -1 depending on the signs in the J-matrix. The later may be more useful in practical implications. How to deal with the close energy band at the end of the anneal is an interesting topic for future work.
In the end we want to summarize the results. Using a modified local field as the initial Hamiltonian, reverse annealing can outperform quantum annealing. We can improve the method further by a quadratic drive of the constraint Hamiltonian. With the changed schedule the energy gap occurs later than in the linear drive. It also increases the size of the gap. The simulations where we reached the biggest energy gap are the same where we reached the lowest energy variance.

Bibliography

1. Kadowaki, T. & Nishimori, H. Quantum annealing in the transverse Ising model. *Phys. Rev. E* **58,** 5355–5363 (5 Nov. 1998) (cit. on p. 1).
2. Hauke, P., Katzgraber, H. G., Lechner, W., Nishimori, H. & Oliver, W. D. *Perspectives of quantum annealing: Methods and implementations* 2019. arXiv: 1903.06559 [quant-ph] (cit. on pp. 1, 5, 6).
3. Choi, V. *Adiabatic Quantum Algorithms for the NP-Complete Maximum-Weight Independent Set, Exact Cover and 3SAT Problems* 2010. arXiv: 1004.2226 [quant-ph] (cit. on p. 1).
4. Farhi, E. *et al.* A Quantum Adiabatic Evolution Algorithm Applied to Random Instances of an NP-Complete Problem. *Science* **292,** 472–475. ISSN: 1095-9203 (Apr. 2001) (cit. on p. 1).
5. Babbush, R., Love, P. J. & Aspuru-Guzik, A. Adiabatic Quantum Simulation of Quantum Chemistry. *Scientific Reports* **4.** doi:10.1038/srep06603. <https://doi.org/10.1038/srep06603> (2014) (cit. on p. 1).
6. Marzec, M. in *Handbook of High-Frequency Trading and Modeling in Finance* 73–106 (John Wiley & Sons, Ltd, 2016). ISBN: 9781118593486. doi:10.1002/9781118593486.ch4. eprint: https://onlinelibrary.wiley.com/doi/pdf/10.1002/9781118593486.ch4. <https://onlinelibrary.wiley.com/doi/abs/10.1002/9781118593486.ch4> (cit. on p. 1).
7. Adachi, S. H. & Henderson, M. P. *Application of Quantum Annealing to Training of Deep Neural Networks* 2015. arXiv: 1510.06356 [quant-ph] (cit. on p. 1).
8. Lloyd, S., Mohseni, M. & Rebentrost, P. *Quantum algorithms for supervised and unsupervised machine learning* 2013. arXiv: 1307.0411 [quant-ph] (cit. on p. 1).
9. Perdomo-Ortiz, A., Dickson, N., Drew-Brook, M., Rose, G. & Aspuru-Guzik, A. Finding low-energy conformations of lattice protein models by quantum annealing. *Scientific Repors* **2,** 571. ISSN: 2045-2322 (Aug. 2012) (cit. on p. 1).
10. Babej, T., Ing, C. & Fingerhuth, M. *Coarse-grained lattice protein folding on a quantum annealer* 2018. arXiv: 1811.00713 [quant-ph] (cit. on p. 1).
11. Kadowaki, T. & Nishimori, H. Quantum annealing in the transverse Ising model. *Phys. Rev. E* **58,** 5355–5363 (5 Nov. 1998) (cit. on pp. 1, 5).
12. Ronnow, T. F. *et al.* Defining and detecting quantum speedup. *Science* **345,** 420–424. ISSN: 1095-9203 (June 2014) (cit. on p. 1).
13. Amin, M. H. Searching for quantum speedup in quasistatic quantum annealers. *Phys. Rev. A* **92,** 052323 (5 Nov. 2015) (cit. on p. 1).

14. Mandrà, S., Zhu, Z., Wang, W., Perdomo-Ortiz, A. & Katzgraber, H. G. Strengths and weaknesses of weak-strong cluster problems: A detailed overview of state-of-the-art classical heuristics versus quantum approaches. *Physical Review A* **94.** ISSN: 2469-9934. doi:10.1103/physreva.94.022337. <http://dx.doi.org/10.1103/PhysRevA.94.022337> (Aug. 2016) (cit. on p. 1).

15. Shin, S. W., Smith, G., Smolin, J. A. & Vazirani, U. *How "Quantum" is the D-Wave Machine?* 2014. arXiv: 1401.7087 [quant-ph] (cit. on p. 1).

16. Santra, S., Quiroz, G., Steeg, G. V. & Lidar, D. A. Max 2-SAT with up to 108 qubits. *New Journal of Physics* **16,** 045006 (Apr. 2014) (cit. on p. 1).

17. Albash, T., Vinci, W., Mishra, A., Warburton, P. A. & Lidar, D. A. Consistency tests of classical and quantum models for a quantum annealer. *Phys. Rev. A* **91,** 042314 (4 Apr. 2015) (cit. on p. 1).

18. Perdomo-Ortiz, A., Venegas-Andraca, S. & Aspuru-Guzik, A. A study of heuristic guesses for adiabatic quantum computation. *Quantum Information Processing* **10,** 33–52 (Jan. 2008) (cit. on pp. 1, 7).

19. Ohkuwa, M., Nishimori, H. & Lidar, D. A. Reverse annealing for the fully connected p-spin model. *Physical Review A* **98.** ISSN: 2469-9934. doi:10.1103/physreva.98.022314. <http://dx.doi.org/10.1103/PhysRevA.98.022314> (Aug. 2018) (cit. on pp. 1, 7).

20. Denchev, V. S. *et al.* What is the Computational Value of Finite-Range Tunneling? *Phys. Rev. X* **6,** 031015 (3 Aug. 2016) (cit. on p. 4).

21. Chancellor, N. Modernizing quantum annealing using local searches. *New Journal of Physics* **19,** 023024 (Feb. 2017) (cit. on pp. 4, 8).

22. Binder, K. & Young, A. P. Spin glasses: Experimental facts, theoretical concepts, and open questions. *Rev. Mod. Phys.* **58,** 801–976 (4 Oct. 1986) (cit. on p. 5).

23. Lucas, A. Ising formulations of many NP problems. *Frontiers in Physics* **2,** 5. ISSN: 2296-424X (2014) (cit. on p. 5).

24. Born, M. & Fock, V. Beweis des Adiabatensatzes. *Zeitschrift für Physik* **51,** 165–180. ISSN: 0044-3328 (Mar. 1928) (cit. on pp. 5, 6).

25. Feshbach, H. Quantum Mechanics. vol. 1. Albert Messiah. Translated by G. M. Temmer. North-Holland, Amsterdam; Interscience, New York, 1961. xv + 504 pp. Illus. 15. *Science* **136,** 514–514. ISSN: 0036-8075 (1962) (cit. on pp. 5, 6).

26. Amin, M. H. S. Consistency of the Adiabatic Theorem. *Physical Review Letters* **102.** ISSN: 1079-7114. doi:10.1103/physrevlett.102.220401. <http://dx.doi.org/10.1103/PhysRevLett.102.220401> (June 2009) (cit. on p. 6).

27. Lidar, D. A., Rezakhani, A. T. & Hamma, A. Adiabatic approximation with exponential accuracy for many-body systems and quantum computation. *Journal of Mathematical Physics* **50,** 102106. ISSN: 1089-7658 (Oct. 2009) (cit. on p. 6).

28. Sachdev, S. *Quantum Phase Transitions* ISBN: 9781139064583 (Cambridge: Cambridge University Press, 1999) (cit. on pp. 6, 7).

29. Nishimori, H. & Ortiz, G. *Elements of Phase Transitions and Critical Phenomena* ISBN: 9780198754084 (Oxford Graduate Texts, 2015) (cit. on p. 7).

30. Susa, Y. *et al.* Quantum annealing of the p-spin model under inhomogeneous transverse field driving. *Physical Review A* **98.** ISSN: 2469-9934. doi:10.1103/physreva.98.042326. <http://dx.doi.org/10.1103/PhysRevA.98.042326> (Oct. 2018) (cit. on p. 7).

31. Yamashiro, Y., Ohkuwa, M., Nishimori, H. & Lidar, D. A. Dynamics of reverse annealing for the fully connected p-spin model. *Physical Review A* **100.** ISSN: 2469-9934. doi:10.1103/physreva.100.052321. <http://dx.doi.org/10.1103/PhysRevA.100.052321> (Nov. 2019) (cit. on p. 7).

32. Reverse Annealing for Local Refinement of Solutions. *D-Wave White Paper Series* (2017) (cit. on p. 8).

33. Lechner, W., Hauke, P. & Zoller, P. A quantum annealing architecture with all-to-all connectivity from local interactions. *Science Advances* **1.** doi:10.1126/sciadv.1500838. eprint: https://advances.sciencemag.org/content/1/9/e1500838.full.pdf. <https://advances.sciencemag.org/content/1/9/e1500838> (2015) (cit. on pp. 8, 9).

34. Seki, Y. & Nishimori, H. Quantum annealing with antiferromagnetic fluctuations. *Phys. Rev. E* **85,** 051112 (5 May 2012) (cit. on p. 10).

35. Ohkuwa, M., Nishimori, H. & Lidar, D. A. Reverse annealing for the fully connected *p*-spin model. *Phys. Rev. A* **98,** 022314 (2 Aug. 2018) (cit. on pp. 10, 13).

36. Hartmann, A. & Lechner, W. Quantum phase transition with inhomogeneous driving in the Lechner-Hauke-Zoller model. *Phys. Rev. A* **100,** 032110 (3 Sept. 2019) (cit. on pp. 13, 17, 32).

37. Johansson, J., Nation, P. & Nori, F. QuTiP: An open-source Python framework for the dynamics of open quantum systems. *Computer Physics Communications* **183,** 1760–1772. ISSN: 0010-4655 (Aug. 2012) (cit. on p. 20).

38. Johansson, J., Nation, P. & Nori, F. QuTiP 2: A Python framework for the dynamics of open quantum systems. *Computer Physics Communications* **184,** 1234–1240. ISSN: 0010-4655 (Apr. 2013) (cit. on p. 20).

39. Susa, Y. & Nishimori, H. *Performance enhancement of quantum annealing under the Lechner-Hauke-Zoller scheme by non-linear driving of the constraint term* 2019. arXiv: 1911.08116 [quant-ph] (cit. on pp. 27, 45).

List of Figures